BioNanoScience
https://doi.org/10.1007/s12668-024-01536-4

RESEARCH

Fabrication of Magnetite Nanoparticles as a Potential Photocatalytic Agent with Cytotoxicity Response

Apurva P. Patil[1] · Pranoti A. Kamble[1] · Arpita Pandey-Tiwari[1] · Umesh V. Shembade[2] · Annasaheb V. Moholkar[2] · Vishwajeet M. Khot[3] · Abhinandan R. Patil[4]

Accepted: 7 July 2024

Abstract

Magnetite (Fe_3O_4) nanoparticles were synthesized using the chemical co-precipitation method and analyzed through XRD, SEM, EDS, and FTIR. The XRD pattern revealed the presence of Fe_3O_4 structural nanocrystals in the iron oxide nanoparticles. SEM images displayed spherical-shaped particles on the surface. EDS spectra indicated the presence of iron and oxygen peaks without impurities. The purity of Fe_3O_4-NPs was confirmed by distinct peaks in the FTIR spectrum. Additionally, the antibacterial activity of Fe_3O_4-NPs was tested against pathogenic bacteria, showing moderate effectiveness against Gram-positive and Gram-negative strains, suggesting potential applications in the biomedical and pharmaceutical sectors. The MTT assay indicated strong anticancer properties of the nanoparticles on colon cancer cell lines (HT29) and normal cell lines (L929). Apoptosis was observed through DAPI staining. The nanoparticles demonstrated a 63.78% scavenging ability through DPPH activity. Moreover, the particles showed the ability to degrade carcinogenic dyes, with a reduction in toxicity observed in the brine shrimp lethality assay, indicating promising biomedical applications.

Apurva P. Patil is the first author, Pranoti A. Kamble and Arpita Pandey-Tiwari are the second authors, and Umesh V. Shembade and Annasaheb V. Moholkar are the third authors of this work.

Highlights

- Fe_3O_4-NPs were proven to be effective photocatalysts for the degradation of carcinogenic dyes.
- $^{\cdot}OH$ radicals were generated on the surface of Fe_3O_4-NPs by sunlight irradiation.
- *In vitro* anticancer activity was exhibited by Fe_3O_4-NPs as a potential mediator for targeted cancer treatment.
- Apoptosis induction by Fe_3O_4-NPs was analyzed by DAPI.
- The CAM examination for angiogenesis revealed considerable blood vessel development.

✉ Vishwajeet M. Khot
Wish.khot@gmail.com

✉ Abhinandan R. Patil
abhisirdyp@gmail.com

[1] Department of Medical Biotechnology and Stem Cells and Regenerative Medicine, Centre for Interdisciplinary Research, D. Y. Patil Education Society, (Institution Deemed to Be University), Kolhapur, Maharashtra 416 006, India

[2] Thin Film Nanomaterials Laboratory, Department of Physics, Shivaji University, Kolhapur, Maharashtra 416 004, India

[3] Department of Medical Physics, Centre for Interdisciplinary Research, D. Y. Patil Education Society, (Institution Deemed to Be University), Kolhapur, Maharashtra 416 006, India

[4] D. Y. Patil College of Pharmacy Kolhapur, D. Y. Patil Education Society, (Institution Deemed to Be University), Kolhapur, Maharashtra 416 006, India

Published online: 29 July 2024

Graphical Abstract

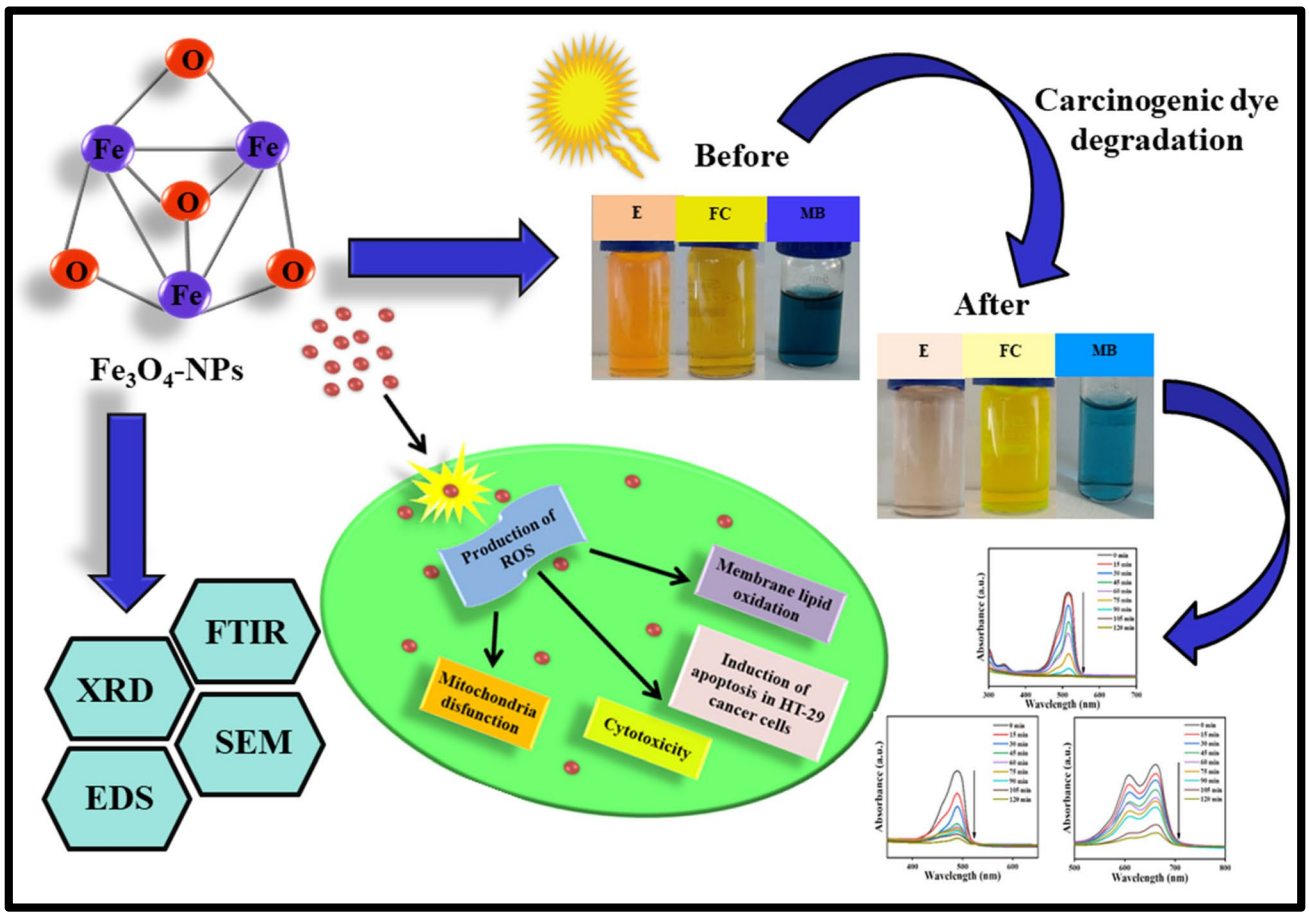

Keywords Angiogenesis · Apoptosis · Carcinogenic dye degradation · Co-precipitation · Cytotoxicity · Inhibitory effect

Abbreviations

BET	Brunauer-Emmett-Teller
CAM	Chick chorioallantoic membrane
Conc.	Concentration
DMEM	Dulbecco's modified Eagle medium
DPPH	2, 2-Diphenyl-1-picrylhydrazyl
DDW	Double distilled water
DLS	Dynamic light scattering
DMSO	Dimethyl sulfoxide
DAPI	4,6-Diamidino-2-phenylindole
E. coli	*Escherichia coli*
EDS	Electron dispersive spectroscopy
E	Eosin
Fe_3O_4	Magnetite
FTIR	Fourier transform infrared spectroscopy
FC	Fluorescein cyanine
MNPs	Magnetic nanoparticles
MTT	3-(4,5-Dimethylthiazol-2-yl)-2,5-diphenyltetrazolium bromide
MB	Methylene blue
NPs	Nanoparticles
NaOH	Sodium hydroxide
NA	Nutrient agar
PBS	Phosphate buffer saline
SEM	Scanning electron microscopy
S. aureus	*Staphylococcus aureus*
UV-VIS	Ultraviolet spectroscopy
VSM	Vibrating sample magnetometer
XRD	X-ray powder diffraction

1 Introduction

Nanoscience and nanotechnology have opened up new possibilities in every field of science and technology [1]. It is a multidisciplinary field that includes physics, biology, biochemistry, engineering, chemistry, and materials science. Nanoparticles have a wide range of applications, including

biomedicine, medication delivery, material chemistry, and control of pollution [2]. Iron oxide nanoparticles (IONPs) are a kind of smart magnetic material with small particle size and large specific surface area. They are smart magnetic materials with low toxicity in biological systems. And it is an FDA-approved nanomedicine. Fe_3O_4 and α-Fe_2O_3 are the most commonly used nanomaterials in this category [3, 4]. One of the most important IONPs is magnetite (Fe_3O_4), which is more widely used than other magnetic nanomaterials due to its biocompatibility. Fe_3O_4-NPs have a cubic inverse spinel structure. This structure gives it special properties so that it can be used in many medical, pharmaceutical, and therapeutic applications. Numerous studies have been conducted in recent years to synthesize Fe_3O_4-NPs, focusing on efficient methods for controlling size, stability, biocompatibility, and achieving monodispersed [5]. Among these methods, the cost-effective co-precipitation technique has been widely employed for synthesizing iron oxide nanoparticles. This method not only exhibits strong ferromagnetic behavior but also demonstrates reduced sensitivity to oxidation [6]. Coprecipitation is a simple and affordable procedure that can be carried out in safe environments without the need for hazardous solvents [7]. The synthesis process relies on various factors, including pH, temperature, type of salt used, and ionic strength, to produce nanoparticles of the desired size and shape [8].

The quality of surface waters is getting worse every day because of the direct discharge of highly hazardous and chemically stable azo dyes from numerous industries into water bodies. These dyes are mutagenic, teratogenic, and carcinogenic, posing significant environmental and health risks [9] and [10]. They are used in the textiles, plastics, and cosmetics industries, which are difficult to break down using traditional wastewater treatment procedures because of their complex chemical structures and resistance to biological breakdown. The release of these dyes into water bodies can cause ecological imbalances and health hazards for both humans and aquatic organisms [11]. One technique that has shown promise for removing hazardous dyes from wastewater is photocatalysis. Photocatalysis has shown promise in removing hazardous dyes from wastewater, but traditional methods are expensive, inaccessible, and sometimes unsuccessful [12]. Scientists are now exploring photodegradation as a more feasible and efficient alternative [13]. Nanomaterial-based photocatalysts like iron (II, III) oxide Fe_3O_4-NPs exhibit high surface area, magnetic responsiveness, and catalytic activity [14], facilitating the efficient degradation of carcinogenic dyes [15]. One mechanism involves the generation of reactive oxygen species (ROS) on the surface of Fe_3O_4-NPs, which exhibit strong oxidizing properties, leading to the degradation of dye molecules [16]. Fe_3O_4-NPs can also serve as electron acceptors or catalysts in redox reactions, facilitating the decomposition of dye molecules into harmless by-products. Their magnetic properties further enhance their utility by allowing easy separation from the reaction mixture using an external magnetic field, simplifying the purification process, and enabling their reuse [17].

Fe_3O_4-NPs indeed possess multifaceted properties that make them intriguing for various applications, including biomedicine and environmental science. Their photocatalytic activity is just one aspect of their versatility [18]. In cancer research, these nanoparticles have been extensively studied due to their potential for targeted drug delivery [19], hyperthermia therapy [20], and imaging modalities such as magnetic resonance imaging (MRI) [21]. Regarding colon cancer, investigations into the cytotoxic effects of iron oxide nanoparticles offer valuable insights into their potential as therapeutic agents. Their ability to induce reactive oxygen species (ROS) generation can selectively target cancer cells while sparing healthy tissue, a crucial aspect in minimizing side effects in cancer therapy [22]. Additionally, the disruption of cellular processes by these nanoparticles further underscores their potential as anti-cancer agents. The evaluation of magnetite nanoparticles in brine shrimp lethality assays serves a dual purpose. Firstly, it provides a rapid and cost-effective means of assessing the potential toxicity of these nanoparticles, thereby informing risk assessments of their environmental impact [23]. Secondly, it aids in understanding the broader ecological implications of nanoparticle contamination in aquatic ecosystems, including effects on organisms higher up the food chain [24].

This study presents a dual novelty focusing on the application of Fe_3O_4-NPs: first, in the degradation of carcinogenic dyes through advanced photocatalytic processes, and second, in the evaluation of their biomedical potential via cytotoxicity studies. These two approaches are the base for ideal anticancer mediators. Further, the fabrication approach focuses on improving nanoparticle efficiency in catalytic processes, with the potential for further environmental remediation and biomedical applications. Integrating these assessments provides a thorough knowledge of the nanoparticles' dual functionality and effective photocatalysis combined with a strong safety profile, highlighting their potential for a wide range of practical applications. This multidisciplinary investigation contributes novel insights into the multifunctional capabilities of Fe_3O_4-NPs, promising advancements in both environmental sustainability and healthcare technology.

The current work aims to solve all limitations that the previous work stated, adding to the significance of the current work after understanding the significance of Fe_3O_4-NPs in biomedical fields. This study exhibits the synthesis of Fe_3O_4-NPs through the co-precipitation method. It takes less time and does not require an expensive chemical as compared to the other synthesis methods listed in Table 1. The study also investigates the antibacterial behavior, antioxidant and cytotoxic activities, carcinogenic dye degradation,

Table 1 A comparison of Fe_3O_4-NPs synthesis techniques, limitations, and applications

Sr. no	Nanoparticles	Synthesis method	Limitations	Application	Refs
1	PEG-coated Fe_3O_4-NPs	Hydrothermal reaction	High reaction temperature longer reaction time, high pressure	Cytotoxicity and magnetic hyperthermia	[25]
2	Silica-coated	Macroemulsion method	Poor yield, a large number of solvents are required, and time-consuming	Antimicrobial activity	[26]
3	Fe_3O_4 stabilized ZrO_2 NPs	Sol–gel reaction	Long reaction time, relatively expensive	Hemolytic activity and antioxidant activity	[27]
4	Gallic acid-coated Fe_3O_4-NPs	Sonochemical method	High temperature and pressure	Drug delivery	[28]
5	Fe_3O_4-NPs	Thermal decomposition	High reaction time	Magnetic resonance imaging	[29]
6	Fe_3O_4-NPs	Co-precipitation	Cost-effective, easy to synthesize	Carcinogenic dye degradation anticancer, angiogenesis, antioxidative, and antimicrobial	Present study

and anti-angiogenesis effects of the synthesized Fe_3O_4-NPs. The NPs were tested against *S. aureus* and *E. coli* strains to determine their effectiveness in inhibiting bacterial growth. Fe_3O_4-NPs exhibited a biocompatible strategy in chick embryos due to their angiogenic properties. The cytotoxicity of the NPs was assessed using human colon carcinoma cell lines (HT-29) and normal fibroblast cell lines (L929), providing insights into their potential as a therapeutic agent for cancer treatment. And also, cell apoptosis and determination of nuclei morphology by 4,6-diamidino-2-phenylindole (DAPI) staining. Fe_3O_4-NPs play a crucial role as an essential antioxidant in the fight against free radicals. The 1,1-diphenyl-2-picryl hydrazyl (DPPH) test is used to study the mechanism of anti-oxidation, which involves scavenging free radicals. The study also reveals promising carcinogenic dye degradation activity. Fe_3O_4-NPs can degrade carcinogenic dyes like methylene blue, fluorescein cyanine, and eosin under natural sunlight. Degrading these dyes naturally is crucial for preventing cancer. Fe_3O_4-NPs act as photocatalysis in the process of carcinogenic dye degradation.

2 Experimental Design

2.1 Materials

Ferric chloride hexahydrate ($FeCl_3.6H_2O$) and ferric chloride tetrahydrate ($Fecl_2.4H_2O$) (≥ 99% AR grade, Sigma-Aldrich, Maharashtra, India) were used as the precursors. Sodium hydroxide (NaOH) (≥ 99% AR grade, Hi-Media, Maharashtra, India) was used as the precipitating agent. Nutrient agar (NA) (≥ 99% AR grade, Hi-Media, Maharashtra, India), phosphate buffer solution (PBS), nutrient broth (NA), ampicillin solution, ascorbic acid, and chemical dyes such as fluorescein cyanine (FC), methylene blue (MB), eosin (ES), 2, 2-Diphenyl-1-picrylhydrazyl (DPPH), 3-(4,5-Dimethylthiazol-2-yl)-2,5-diphenyltetrazolium bromide (MTT), 4,6-diamidino-2-phenylindole (DAPI), and Dimethyl sulfoxide (DMSO) were purchased from (≥ 99% AR grade, Hi-Media, Maharashtra, India). Deoxygenated distilled water (DDW) was consistently utilized in all experiments and for nanoparticle synthesis.

2.2 Synthesis of Magnetite Nanoparticles

The co-precipitation technique is commonly used to synthesize pure magnetite nanoparticles, as shown in Scheme 1. In this method, ferric chloride hexahydrate ($FeCl_3.6H_2O$) and ferric chloride tetrahydrate ($Fecl_2.4H_2O$) are dissolved in DDW and stirred at 70 °C for 30 min. After 30 min, a dropwise solution of NaOH was added to maintain a pH of 13.0. After the addition of NaOH solution, the color changes from orange to black which indicates the formation of Fe_3O_4-NPs successfully. These nanoparticles are then separated using a magnet, rinsed with DDW to remove salts, and then dried in an oven at 70 °C for 12 h. The resulting Fe_3O_4-NPs are converted into black powder for further use [30].

2.3 Characterization

Confirmation of the formation of Fe_3O_4-NPs was visually achieved by observing the color change in the reaction mixture. The crystalline nature of the synthesized material was then determined by analyzing the XRD patterns of the NPs obtained using a Rigaku 600 Mini Flex Japan instrument. Fourier transform infrared (FTIR) spectra recorded with a LAMBADA-7600 spectroscopy were utilized to analyze the structural and bonding information of the surface-modified NPs. The surface morphology was evaluated through scanning electron microscopy and energy-dispersive X-ray spectroscopy using the JEOL JSM-IT200 Japan model. Particle size distribution statistics were examined

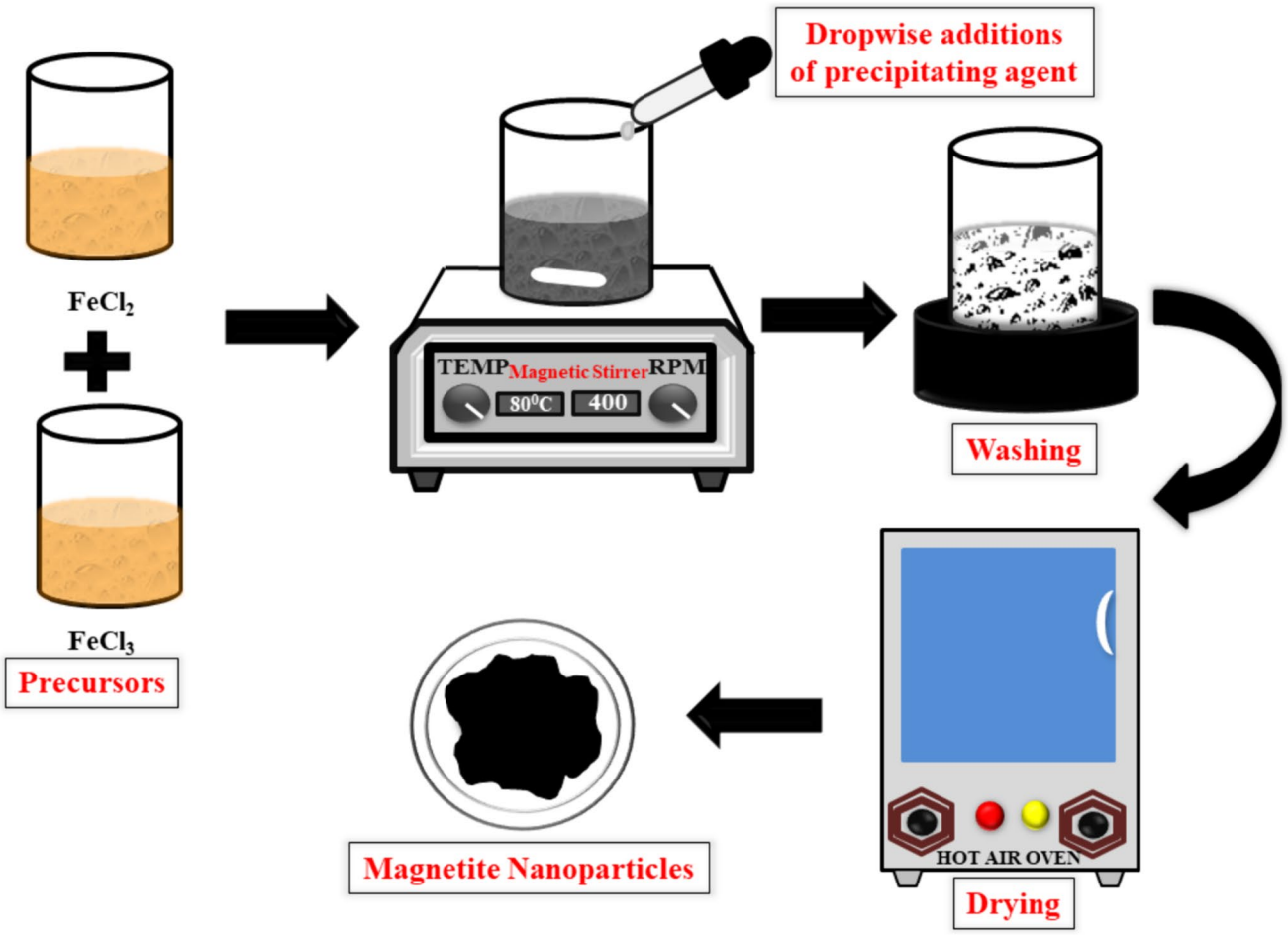

Scheme 1 Schematic representation of the synthesis process of Fe_3O_4-NPs by the co-precipitation method

using ImageJ software. Further analysis of the synthesized material involved dynamic light scattering (DLS) and zeta potential analysis using the Malvern Zeta Nano S90 instrument. Magnetic characteristics were assessed using a vibration sample magnetometer (VSM). The UV–visible absorption spectra of the synthesized Fe3O4-NPs were measured using an Agilent Technology Cary-60 UV–visible spectrophotometer. Evaluation of the size of the pores and specific surface area of the Fe_3O_4-NPs was carried out through Brunauer–Emmett–Teller (B BET) analysis using the Micromeritics USA model ASAP2010.

2.4 Carcinogenic Dye Degradation

The aim of this study was to examine the degradation of carcinogenic dyes using synthesized Fe_3O_4-NPs under natural sunlight exposure. The experiment involved three different carcinogenic dyes: methylene blue (MB), fluorescein cyanine (FC), and eosin (E). Each dye was prepared in a 0.1% aqueous solution. Initially, the dyes were mixed with the Fe3O4-NPs and allowed to stir in darkness for 30 min to establish adsorption and desorption equilibrium. Subsequently, the solution was exposed to natural sunlight for a specific duration, and the extent of degradation was measured using a UV–visible spectrometer. The percentage of carcinogenic dye degradation was calculated using the following formula:

$$\% \text{ degradation } = \frac{A0 - At}{A0} \times 100$$

where A_0 is the absorbance before irradiation and A_t is the absorbance at time t. The absorbance contributed by nanoparticles was subtracted from the test solution (kept as a control) in the experiment [31].

2.5 In Vitro Cytotoxicity Studies of Fe_3O_4-NPs on Colon Cancer Cells

The in vitro cytotoxicity studies of Fe_3O_4-NPs were investigated by using human colon carcinoma cell lines (HT-29) and normal fibroblast cell lines (L929). Cell suspensions were seeded in a 96-well plate with DMEM and 5% fetal bovine

serum and incubated overnight at 37 °C and 95% humidity. Cells were treated with Fe_3O4-NPs at several doses (10, 40, 60, and 100 µg/ml) and incubated at 37 °C for 24 h in a 5% CO_2 incubator. After 24 h, cells were washed with PBS for washing purposes. Then, each cell was stained with 20 µL of MTT solution and incubated at 37 °C for 24 h. Subsequently, 100 µL of DMSO was used to dissolve the formazan, and absorbance was evaluated by using a plate reader at 570 nm. The viable cell quantity was determined in triplicates [32].

2.6 Nuclei Visualization with DAPI Fluorescence

In this experiment, the L929 and HT29 cell lines were cultivated in 24-well plates at a density of 1×10^5 cells per well. The culture medium employed was DMEM, supplemented with the appropriate concentration of synthesized Fe_3O_4-NPs. As a control group, cells without Fe_3O_4-NPs were also included. The cells were then incubated at a temperature of 37 °C for a period of 24 h. Following incubation, the cells were fixed using a 4% paraformaldehyde-PBS solution for 15 min. Subsequently, DAPI staining was carried out at room temperature for 30 min. The nuclear morphology of both cell types was examined using a fluorescence microscope from Olympus, PA, USA. Apoptotic cells exhibited distinct nuclear characteristics, including fragmentation, condensation, and degradation [33].

2.7 In Ovo Cytotoxicity Studies of Fe_3O_4-NPs

The chick chorioallantoic membrane (CAM) assay was utilized to assess the angiogenic efficacy of Fe_3O_4-NPs. Fertilized chicken eggs (0 days) were obtained from a local egg hatchery in Kolhapur, Maharashtra, India. The eggs were sterilized with 70% ethanol and then placed in an egg incubator at 37 °C with 70–80% humidity. After 5 days, a small hole was made at the distal end of the eggs to create a 2-cm^2 window, and 2 mL of albumin was extracted. The correct development of the embryo was confirmed by removing the opposing side shell piece. Whatman filter discs were soaked in PBS as a control, as well as in 2 mg/ml and 5 mg/ml of Fe_3O_4-NPs before being placed on the CAM. The open window was sealed with parafilm, and the eggs were kept in the incubator at 37 °C with 70–80% humidity. Periodically, the parafilm was removed, and the CAM angiogenic capillaries were photographed and analyzed morphologically and geographically using Angio Tool 0.6 software (RRID:SCR_016393) [34].

2.8 Studies on the Lethality of Fe_3O_4-NPs on Brine Shrimp

Artemia salina larvae were subjected to a lethality test within a 24-h timeframe using a 24-well plate. To facilitate hatching, Artemia cysts were cultivated in a brine solution for 24 h. Once hatched, the Artemia larvae were meticulously gathered and placed in separate wells of the 24-well plate. Each well was then populated with 10 Artemia larvae and treated with varying concentrations of Fe_3O_4-NPs (100, 200, 400, 600, 800, and 1000 µg/mL). The plate was subsequently incubated at 37 °C for 24 h. Following the incubation period, the number of surviving organisms in each well was tallied and compared to an untreated control group. This comparison allowed for the calculation of the percentage of mortality induced by the Fe_3O_4-NPs treatment [21].

$$\% \text{ Lethality} = \frac{\text{Number of dead } \textit{Artemia nauplii}}{\text{Initial number of } \textit{live Artemia nauplii}} \times 100$$

2.9 Free Radical Scavenging Assay of Fe_3O_4-NPs

In order to determine the antioxidant activity of the sample compounds, we assessed their ability to scavenge free radicals using the DPPH method. The Fe_3O_4-NPs test compounds were dissolved in water and prepared in different volumes (20 µL, 40 µL, 60 µL, 80 µL, and 100 µL), which were then placed in a microtiter plate. The control consisted of only the ascorbic acid solution. Subsequently, 100 µL of a 0.1% methanolic DPPH solution was added to each well containing the test compounds. The plate was incubated in darkness for a period of 30 min. Visual examination of the samples was conducted to observe any color changes, with a shift from purple to yellow or pale pink indicating strong or weak positive antioxidant activity, respectively. Finally, the plate was analyzed at a wavelength of 517 nm using an ELISA plate reader [35]. The following formula was used to determine the radical scavenging activity:

$$\text{DPPH radical scavenging activity } (\%) = \frac{[(\text{Absorbance of control} - \text{Absorbance of test sample})}{(\text{Absorbance of control})]} \times 100$$

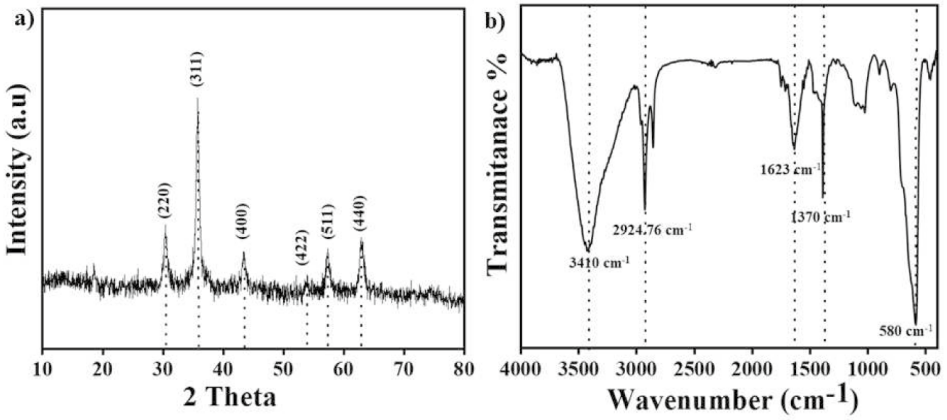

Fig. 1 **a** XRD pattern for the Fe_3O_4-NPs; (**b**) FT-IR spectrum for the Fe_3O_4-NPs

2.10 Inhibitory Effect of Fe_3O_4-NPs on Microbial Growth

The inhibitory effect of the synthesized Fe_3O_4-NPs was evaluated using the agar well diffusion method. Pure cultures of *S. aureus* (ATCC 24923) and *E. coli* (ATCC 25922) were tested for antibiotic susceptibility. Nutrient agar plates were prepared for each strain and inoculated with 1.5×10^6 cells using the spread plate technique. Wells were created with a sterile cork borer, with ampicillin (100 mg/mL) in the first well as a positive control, the test sample with Fe_3O_4-NPs in the second well, and water in the final well as a negative control. The plates were then incubated at 37 °C for various time intervals to observe the zone of inhibition of bacterial growth [36].

2.11 Inhibitory Effect of Fe_3O_4-NPs at Time Interval Method

The optical densities (OD 200–800 nm) of overnight cultures of *E. coli* and *S. aureus* bacteria were measured and diluted to obtain 10^6 CFU/mL bacterial counts. A 200 µL aliquot of the diluted bacterial culture was added into the sterile nutrient broth tube and incubated at 37 °C for 24 h. Next, 2.9% w/v in concentration was added to the Fe_3O_4-NPs tube and the sterile nutrient broth tube, respectively. These two tubes were incubated at 37 °C for 0 h, 6 h, 12 h, 24 h, and 48 h, respectively. After the addition of nanoparticles, immediately start data collection for the growth curve [37].

2.12 Statistical Analysis

Experiments were executed three times, and the results were expressed as the mean value with the standard deviation.

3 Results and Discussion

3.1 Characterization of Fe_3O_4-NPs

The powder X-ray diffraction (XRD) pattern serves as an effective technique in determining the structural phase and crystallite sizes of the synthesized Fe_3O_4-NPs. In Fig. 1a, the XRD pattern reveals an inverse spinel cubic crystal structure (JCPDS card No-19–029) of Fe_3O_4-NPs, with distinct peaks (2θ) observed at diffraction angles of 30.54°, 35.06°, 43.51°, 53.79°, 57.41°, and 62.87° corresponding to indices (220), (311), (400), (422), (511), and (440). The average crystallite size (D) of the synthesized Fe3O4 NPs was calculated using Debye–Scherrer's formula [38].

$$D = \frac{K\lambda}{\beta cos\theta} \tag{1}$$

where β is the line broadening at full width half-maximum (FWHM) in radians, K is the Scherrer constant 0.94 for spherical crystallites with cubic symmetry, λ is the x-ray wavelength $Cuk_\alpha = 1.5406$ A°, θ is the Bragg angle in degrees, half of 2 θ. The average crystallite sizes of the NPs are calculated from the most intense peak (311), using the said equation. The calculated crystallite size of Fe_3O_4-NPs-NPs was found to be 10.37 nm.

The FTIR spectrum of Fe_3O_4-NPs offer crucial insights into the functional groups attached to their surface. The synthesized Fe_3O_4-NPs were analyzed using FTIR spectroscopy, and KBr pellets were prepared for the analysis. In Fig. 1b, the infrared spectra of the Fe_3O_4-NPs displayed bands within the 400–4000 cm^{-1} range, revealing the chemical bonds and functional groups present in the compound. Notably, bands at 3410 cm^{-1}, 2924.76 cm^{-1}, and 1623 cm^{-1} indicated the existence of hydroxyl groups from water molecules on the

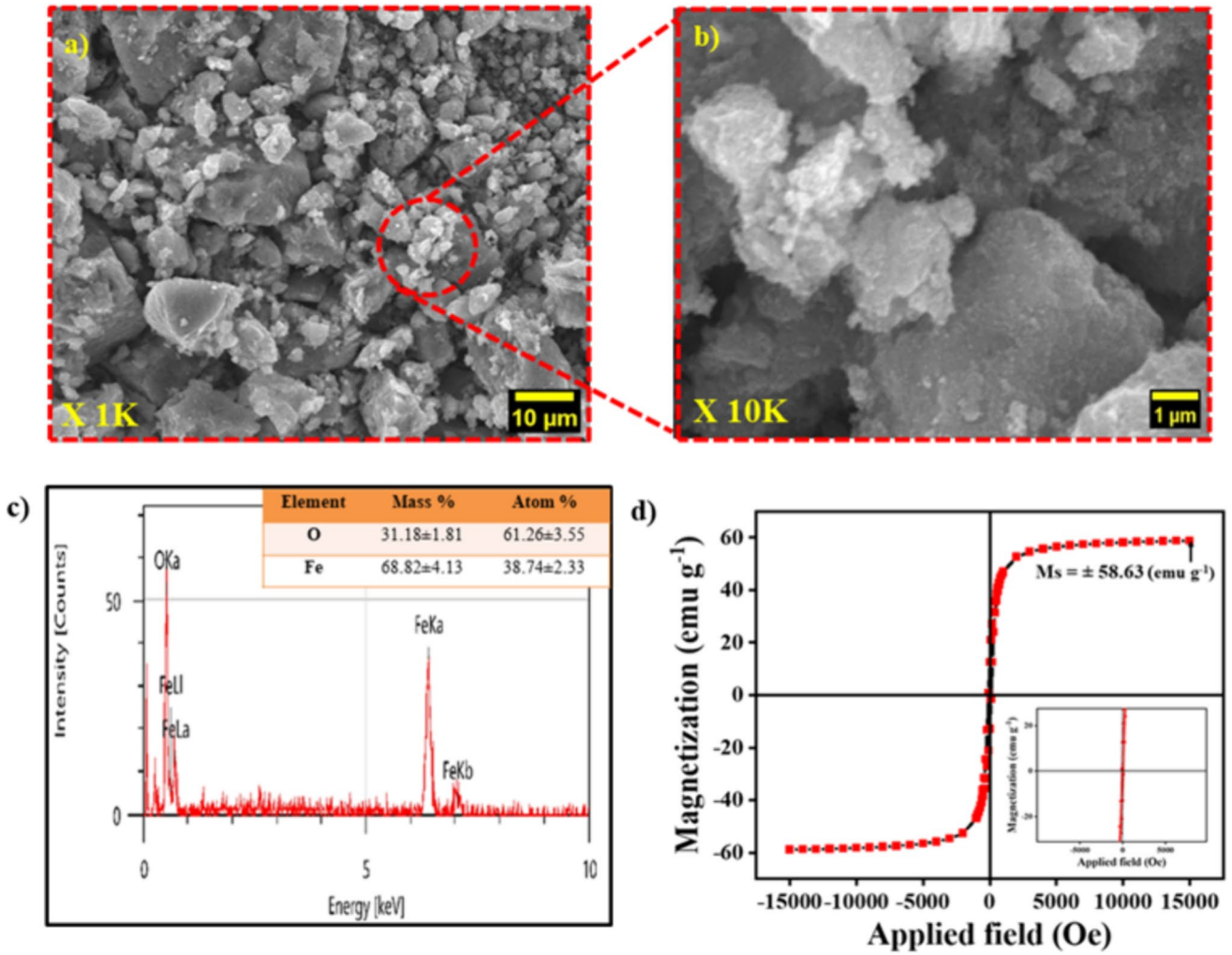

Fig. 2 **a**, (**b**) SEM micrographs of the Fe_3O_4-NPs at low and high magnifications, respectively; (**c**) EDX spectrum of Fe_3O_4-NPs; (**d**) magnetic property of Fe_3O_4-NPs via VSM

nanoparticle surface, with these bands corresponding to bending and stretching vibrations of the hydroxyl groups. Furthermore, distinct bands at 580 cm^{-1} confirmed the synthesis of Fe_3O_4-NPs and their specific bonding arrangement with iron and oxygen atoms [39].

Microscopic examination was carried out on Fe_3O_4-NPs using scanning electron microscopy to analyze their surface morphology. The SEM images presented in Fig. 2a, b clearly demonstrated the quasi-spherical shape of the synthesized Fe_3O_4-NPs, providing insights into the aggregation of ferrite particles. This aggregation phenomenon can be attributed to the presence of nanometer-sized particles, which contribute to the enhancement of both surface energy and magnetic properties of the materials. These nanoparticles exhibit a size distribution ranging from 30 to 35 nm and have a natural tendency to aggregate due to their magnetic nature. The larger particles observed in the SEM images are referred to as secondary particles, formed by the fusion of primary particles with a crystalline structure. To modulate the pH levels, a NaOH solution was utilized to expedite the chemical reactions during the synthesis process. Consequently, an increase in the quantity of NaOH resulted in a higher number of interactions and surface corrosion. The intensified interplay between the magnetic moments of the nanoparticles led to further agglomeration and an augmentation in nanoparticle size [40]. Furthermore, EDX analysis was carried out to validate the chemical composition of the nanoparticles, with Fig. 2c displaying the EDX spectrum of Fe_3O_4-NPs, confirming the presence of Fe and O within the composite structure.

Utilizing a vibrating sample magnetometer (VSM) at room temperature, the synthesized Fe_3O_4-NPs were examined, revealing significant magnetic properties. The magnetization curves (Fig. 2d) display a characteristic s-shaped profile, which is commonly observed in super-paramagnetic materials. This behavior indicates that the Fe_3O_4-NPs are responsive to external magnetic fields but do not retain any

Table 2 Structural and magnetic properties of Fe_3O_4-NPs from XRD and VSM, BET

Sr. no	Sample	Crystallite size nm	Hc (Oe)	Ms (emug^{-1})	Squareness (*S*)	BET (m^2g^{-1})	Pore volume (cm^3g^{-1})	Pore size (nm)
1	Fe_3O_4-NPs	10.37	− 1.5	58.63	0.405	38.17	0.1298	14.31

residual magnetization once the field is removed [41]. When subjected to a 15 kOe magnetic field, Fe_3O_4-NPs display a high magnetic response, reaching a maximum saturation magnetization (Ms) of 58.63 emu g^{-1}. The curves indicate a low coercivity, allowing for magnetization and demagnetization cycles at low magnetic field intensities. These results underscore the suitability of Fe_3O_4-NPs for applications that demand well-defined magnetic characteristics, such as biomedical technology and environmental remediation processes. Table 2 provides the magnetization parameter values.

The size of the synthesized Fe_3O_4-NPs was determined using dynamic light scattering (DLS), a technique that measures the hydrodynamic size of particles in a liquid state. The analysis, presented in Fig. S1a, revealed a size of 98 nm. In a liquid medium, particles exhibit different behavior due to the presence of electrostatic and non-electrostatic interactions on their surfaces. This is why DLS is employed to capture the total size of the particles. Figure S1b displayed the maximum zeta potential of the Fe_3O_4-NPs, which was found to be − 27.81 mV. This indicates that the surface of the Fe_3O_4-NPs is composed of negatively charged molecules that disperse and expand within the medium. The negative zeta potential values contribute to the stability of the Fe_3O_4-NPs dispersion [42].

According to the theory of UV/Vis spectroscopy, the outer electrons of atoms absorb radiant energy and undergo transitions to higher-energy levels. This process results in the production of an absorption spectrum, which can be used to determine the band-gap energy of metal oxides [43]. In the case of Fe_3O_4-NPs, the UV/Vis spectra revealed an absorption band at 294 nm within the visible range of 200–800 nm (Fig. S2a). To calculate the band-gap energies of Fe_3O_4-NPs, Tauc's equation (Eq. 2) was employed. This equation utilizes the absorption coefficient (α), a constant (A) based on the effective electron mass, and a direct transition factor ($r = 0.5$). The straight band-gap rule, expressed as $(\alpha h\nu)^{1/2} = A(h\nu\text{-}Eg)$, where Eg represents the band-gap energy, ν is the frequency, and h is Planck's constant, was applied. To determine the band-gap energy of Fe_3O_4-NPs, a plot of $(\alpha h\nu)^{1/2}$ versus $h\nu$ was generated, and the curve was extrapolated to the axis [44]. 2.33 eV band gap of Fe_3O_4-NPs was obtained through Tauc's equation.

$$(ahv)n = A(hv - Eg) \tag{2}$$

The surface area and pore size distribution of Fe_3O_4-NPs were determined through nitrogen adsorption–desorption isotherms, as depicted in Fig. S3a, b. By employing the multipoint BET method within a relative pressure (P/P0) range of 0.05 to 0.3, the specific surface area of Fe_3O_4-NPs was found to be 38.17 m^2g^{-1}. Furthermore, the Barrett-Joyner-Halenda (BJH) method was utilized to analyze the desorption isotherm and ascertain the pore size distribution, resulting in an average pore size of 14.31 nm and a total pore volume of 0.1298 cm^3g^{-1}. These findings indicate that Fe_3O_4-NPs possess mesoporous characteristics, making them suitable for applications in catalysis and magnetic separations. The comprehensive nature of this characterization highlights the potential of Fe_3O_4-NPs for tailored applications across various fields [45].

3.2 Carcinogenic Dye Degradation

Fe_3O_4-NPs are used to investigate the carcinogenic dye degradation of three possibly cancer-causing dyes: aqueous MB, ES, and FS. This degradation process was run under natural sunlight at different time intervals. Utilizing UV–Vis spectroscopy, the efficacy of Fe_3O_4-NPs as a catalyst for dye degradation was determined [46]. The absorption spectra for each dye were measured between 300 and 800 nm. The largest absorbance peak of MB in the visible region, the largest absorbance peak of MB is located at 660 nm, followed by a shoulder peak at 610 nm. The highest absorbance peaks of ES and FC are obtained at 520 and 490 nm, respectively, as shown in Figs. 3, 4, and 5a. As time increases, the intensity of the absorption spectra decreased [39] due to a redox reaction on the photocatalyst's surface. At the end of the process, 80.30% MB dye was degraded within 120 min. Similarly, the photocatalytic performance of ES and FC is 97.02 and 86.83%, respectively, as shown in Figs. 3, 4, and 5b. The strong linear relationship between ln (C0/C) and time provides evidence for the pseudo-first-order kinetic model (Figs. 3, 4, and 5c). Based on the plot ln (C0/C) versus time shown in Figs. 3, 4, and 5d, the kinetic reaction rate constant (K) calculated from the degradation of the MB, ES, and FS was 0.0078, 0.0156, and 0.0311 min^{-1} with an R^2 value of 0.99, 0.95, and 0.92 respectively.

The mechanism of the carcinogenic dye degradation process using Fe_3O_4-NPs in natural sunlight is shown in Scheme 2. The catalyst, made of magnetite nanoparticles, collects photons and forms electron–hole pairs, causing reactive oxygen species (ROS) to form on its surface. Because of their semiconductor nature and magnetic retrievability, excellent and

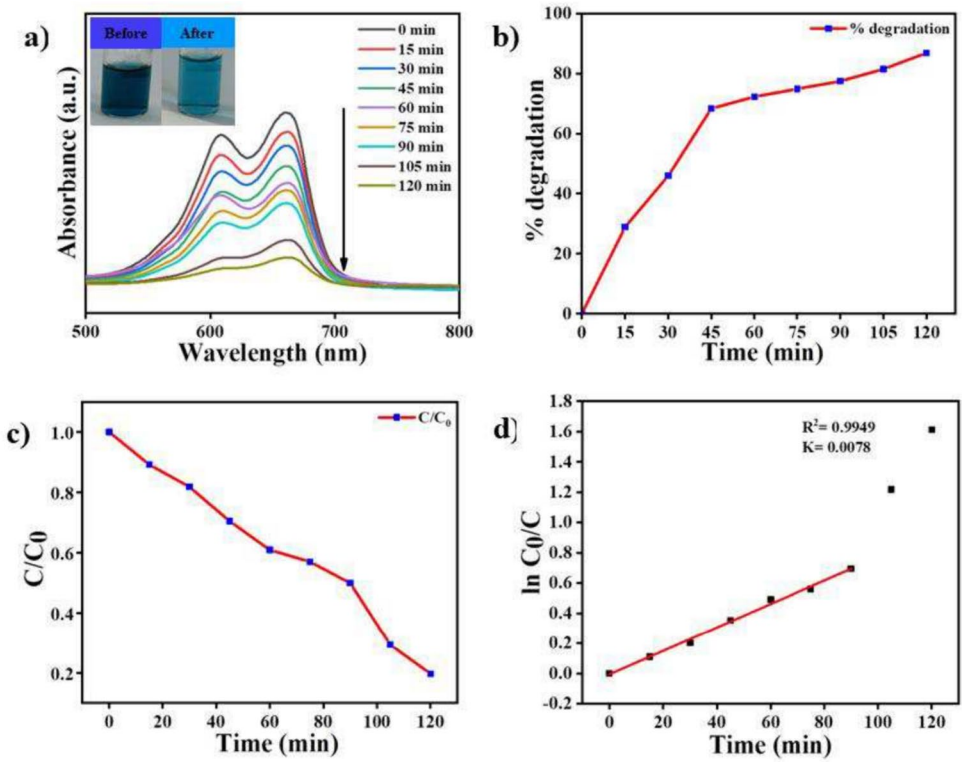

Fig. 3 Carcinogenic dye degradation of MB using Fe_3O_4-NPs: (**a**) UV–vis absorption spectra; (**b**) percentage of dye degradation; (**c**) plots of C/C0 versus time (min) using a photocatalyst; (**d**) kinetic plot of ln C0/C vs. irradiation time for photodegradation of MB dye

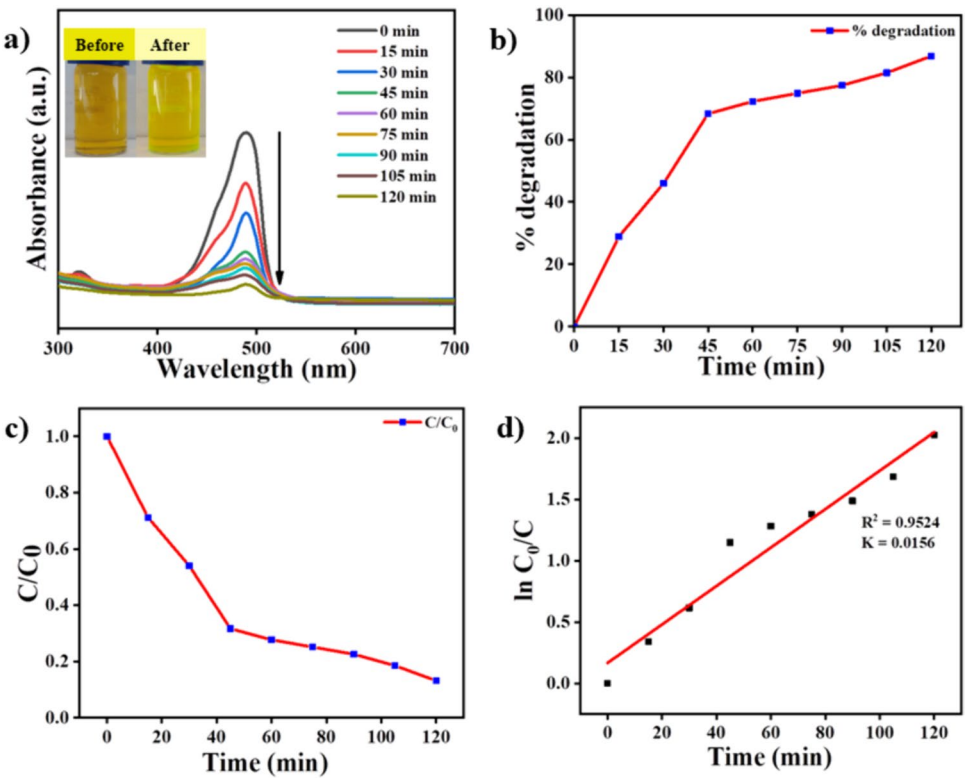

Fig. 4 Carcinogenic dye degradation of FC using Fe_3O_4-NPs: (**a**) UV–vis absorption spectra; (**b**) percentage of dye degradation; (**c**) plots of C/C0 versus time (min) using a photocatalyst; (**d**) kinetic plot of ln C0/C vs. irradiation time for photodegradation of FC dye

recyclable catalysts improve the photocatalytic dye degradation process under natural light. These radicals oxidize organic colors into simpler molecules like carbon dioxide and water. ROS, such as hydroxyl radicals (•OH) and superoxide radicals (•O2 −), may oxidize organic pollutants, including methylene blue, eosin, rhodamine, and fluorescein cyanine dyes, breaking

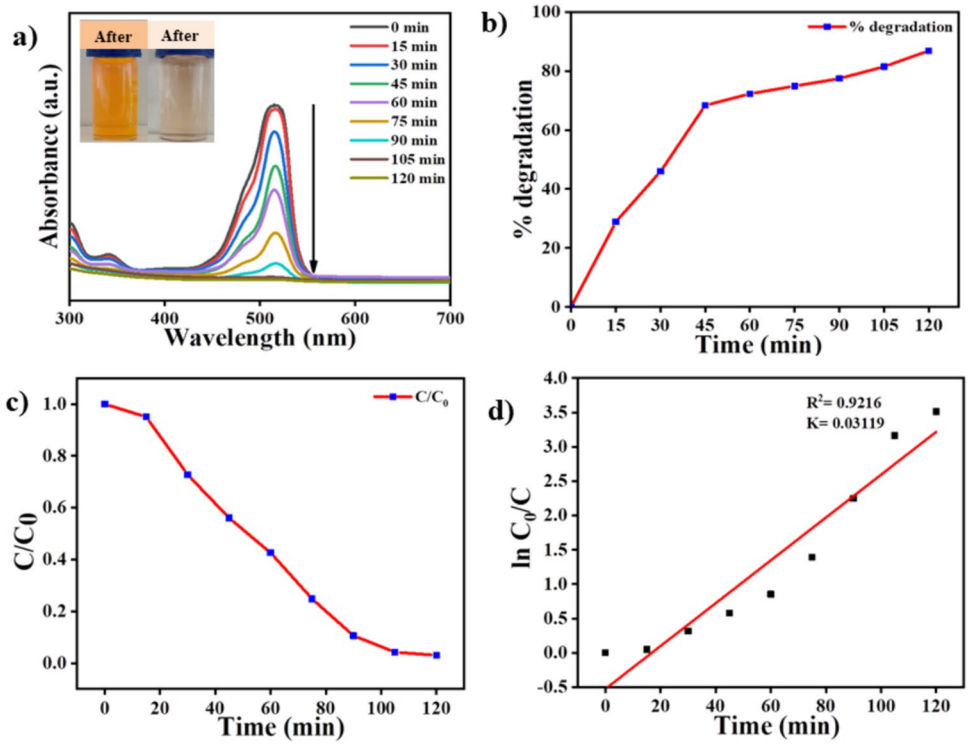

Fig. 5 Carcinogenic dye degradation of E using Fe_3O_4-NPs: (**a**) UV–vis absorption spectra; (**b**) percentage of dye degradation; (**c**) plots of C/C0 versus time (min) using a photocatalyst; (**d**) kinetic plot of ln C0/C vs. irradiation time for photodegradation of FC dye

them down into harmless by-products. Because of their large band gap, magnetite nanoparticles are able to efficiently absorb sunlight. When exposed to natural sunlight, magnetite nanoparticles absorb photons, moving electrons from the valence band to the conduction band and forming electron–hole pairs [47]. The solution's dye molecules adhere to the magnetite nanoparticles' surface. By allowing the dye molecules to be closer to the photocatalytic sites on the surface of the nanoparticle, this adsorption step increases the effectiveness of the degradation process [48]. The magnetite nanoparticles produce electron–hole pairs when they absorb sunlight. These photoexcited electrons and holes undergo redox interactions with water and oxygen molecules adsorbed on the nanoparticle surface, resulting in the production of ROS, mainly •OH. The organic dye molecules adsorbed on the surface of the nanoparticle are targeted by the produced ROS, especially the hydroxyl radicals. This causes the dye molecules to break down into smaller, less toxic compounds, which eventually causes the dye to mineralize. Since magnetite nanoparticles are magnetic, it is easy to remove them from the solution once the degrading process is complete. As a result, the process becomes more economical and ecological. They can afterward be recycled and used again for additional deterioration cycles.

3.3 In Vitro Cytotoxicity Studies of Fe_3O_4-NPs on Colon *Cancer* Cells

The first step in determining the toxicity of NPs is evaluating cell viability. In Fig. 6a, the metabolic activity of HT29 cancer cell lines and L929 normal cell lines was analyzed at different concentrations of Fe_3O_4-NPs (10, 40, 60, and 100 µg/ml) through the MTT test to assess cell viability and cytotoxicity. A colorimetric test was utilized to evaluate cell viability by converting MTT, a yellow tetrazolium salt, into purple formazan crystals. The amount of formazan generated was directly related to the number of metabolically active cells. Absorbance readings at 570 nm using a spectrophotometer showed that higher absorbance values were indicative of enhanced cell survival. This method allowed for the examination of the effects of Fe_3O_4-NPs on cell function and the distinction of cytotoxic impacts between normal and cancer cell types based on metabolic responses. In contrast, the NP-treated HT29 cell lines experienced significant reductions in cell viability. The graph clearly illustrates a decrease in cell viability as the concentration of Fe_3O_4-NPs increases. Figure 6b presents the absorbance of MTT at various concentrations of Fe_3O_4-NPs. After 24 h, it was observed that only 67.24% of HT29 cells remained viable at a concentration of 10 µg/mL. Similarly, the percentages of viable HT29 cells at concentrations of 40, 60, and 100 µg/mL were 62.55%, 45.62%, and 30.22%, respectively. In contrast, when the concentration gradually increased, 98.22%, 93.84%, 82.76%, and 79.09% of normal fibroblast cells remained alive. The Fe_3O_4-NPs exhibit enhanced anticancer activity against colon cancer cells due to their ability to stimulate the production of reactive oxygen species (ROS) within these cancer cells. These ROS generate oxidative stress, leading to the destruction of cellular components and the initiation of cancer

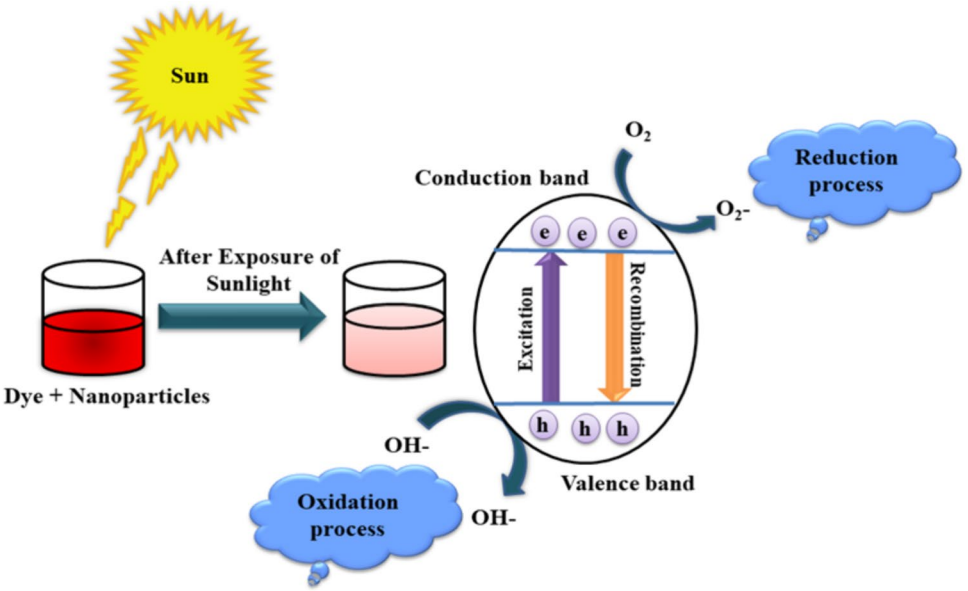

Scheme 2 Mechanism of carcinogenic dye degradation by using nanoparticles in natural sunlight

cell apoptosis, also referred to as programmed cell death. This phenomenon can be explained by the breakdown of Fe_3O_4-NPs into $Fe2^+$ and $Fe3^+$ ions within the cancer cells at a pH level of 4–5. These resulting ions play a crucial role in the generation of ROS by converting H_2O_2 into hydroperoxyl (HOO•) and hydroxyl (HO•) radicals in the mitochondria through Fenton's reaction [49]. Ferroptosis, a form of cell death that depends on iron and is initiated by lipid peroxidation, presents an additional credible explanation. The release of iron can trigger the Fenton reaction, leading to ferroptosis in tumor cells. Moreover, the compact size of Fe_3O_4-NPs enables effective absorption by cells and promotes optimal interaction with cancer cells. The unique magnetic properties of Fe_3O_4-NPs allow for precise targeting of tumors, enhancing treatment effectiveness while reducing damage to surrounding healthy tissues. In general, Fe_3O_4-NPs present a versatile approach to fighting cancer by delivering targeted therapy and ROS-induced cell death, offering promising prospects for cancer treatment. The research analyzed bright-field microscopy pictures of L929 and HT29 cell reactions to Fe_3O_4-NPs at varying doses, depicted in Fig. 6c. The results indicate that L929 cells exhibit minimal influence at both concentrations. However, HT29 cells display clear indications of necrosis when exposed to Fe_3O_4-NPs at higher concentrations of 100 mg/L, suggesting significant cell death. This study suggests that Fe_3O_4-NPs could potentially be employed to selectively target and induce cell death in cancer cells while safeguarding normal cells.

3.4 Nuclei Visualization with DAPI Fluorescence

In cancer cell apoptosis identification, techniques like DAPI staining can reveal condensed and fragmented nuclei, characteristic of apoptotic cells, under fluorescence microscopy. During apoptosis, chromatin condenses and the nucleus fragments, resulting in smaller, intensely stained apoptotic bodies compared to the uniform and intact nuclei of healthy cells. Under fluorescence microscopy, apoptotic cells appear with intensely stained, condensed nuclei that are smaller and irregular, distinguishing them from non-apoptotic cells. Multiple studies have shown that Fe_3O_4-NPs may generate ROS and induce oxidative stress in cancer cells, resulting in DNA damage and apoptotic cell death. In cancer cells, the two signs of apoptosis are abnormal cell size (shrunk and decreased cells) and DNA fragmentation [50]. To confirm apoptotic features, morphological alterations in the colon cancer cell line HT29 were observed, but normal (L929) cells often showed uniformity. Further observational investigations reveal the disintegration of the nucleus into many minute fragments known as apoptotic bodies, confirming cell death by apoptosis. Morphological changes, such as shrinkage and/or an undistinguished shape of the nucleus (Fig. 7e, f), have been observed in HT29 cells with an increasing concentration of Fe_3O_4-NPs as compared to untreated colon cancer cells and normal cells.

3.5 In Ovo Cytotoxicity Studies of Fe_3O_4-NPs on Chick Embryo

In ovo experiments showing no antiangiogenic activity in CAM are a positive indication of their biocompatibility due to their angiogenic effects. The CAM test is a popular model for examining angiogenesis because of its large vascular network and simplicity of observation. Angiogenesis is the process of developing new blood vessels from pre-existing vessels. Fe_3O_4-NPs possess unique magnetic and chemical

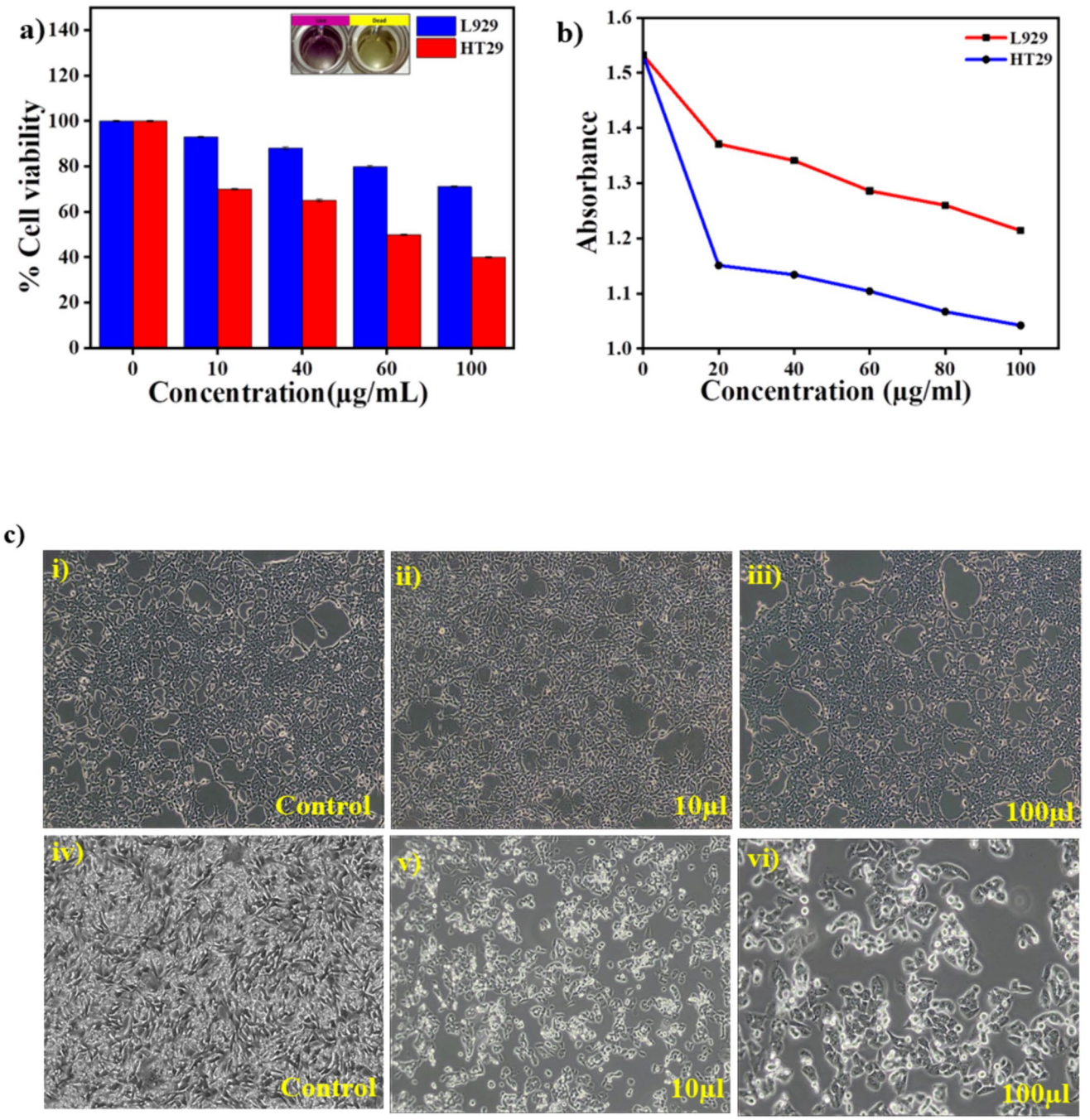

Fig. 6 **a** Bar graph of the MTT cell viability assay; (**b**) MTT absorbance vs. concentration graph; **c** Representative bright-field microscopy images depicting the cell viability of HT29 and L929; (i) control L929 cells; (ii) L929 cells after treatment with NPs at conc. 10 µl; (iii) L929 cells after treatment with NPs at conc. 100 µl; (iv) before control HT29 cells; (v) HT29 cells after treatment with NPs at conc. 10 µl; (vi) HT29 cells after treatment with NPs at conc. 100 µl

characteristics that make them highly suitable for use in CAM. In the present study, the CAM evaluation is utilized to investigate the effects of Fe_3O_4-NPs on angiogenesis. Generally, embryonated eggs were utilized for the CAM test, which took 3–5 days to complete. In the current investigation, the eggs were treated with varied concentrations (2 mg/mL) and (5 mg/mL) of Fe_3O_4-NPs, as well as PBS as a control. The study compared the angiogenic properties of synthesized Fe_3O_4-NPs in CAM, revealing that the treatment group with 2 mg/mL and 5 mg/mL Fe_3O_4-NPs formed new blood vessels, demonstrating efficient angiogenic properties, and histological analysis using HE staining

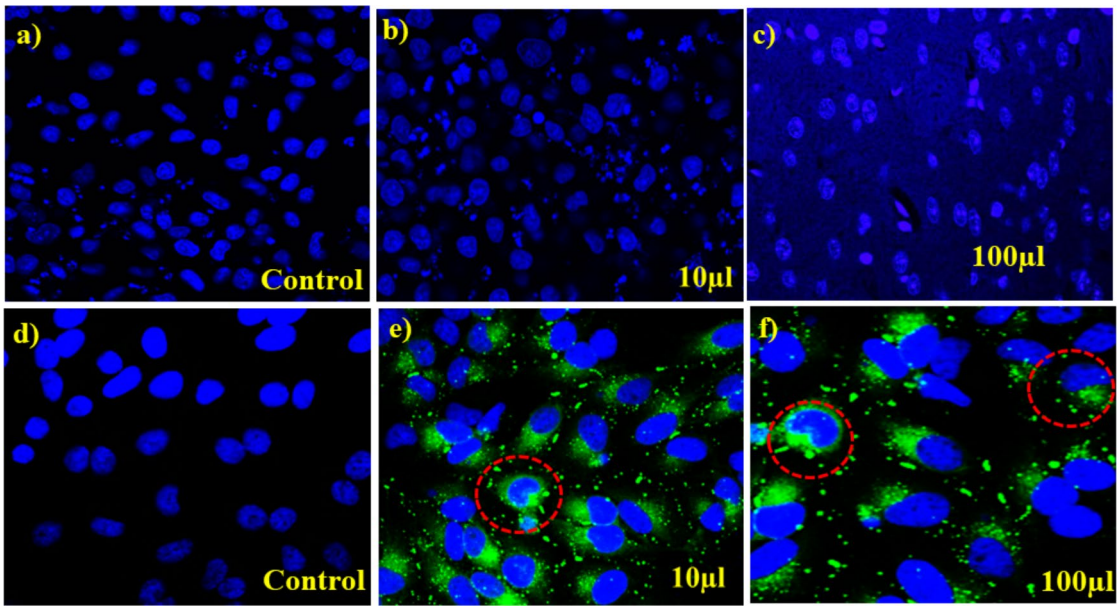

Fig. 7 DAPI-stained fluorescence images of L929 and colon HT29 cells: (**a**) untreated L929 cells; (**b**) L929 cells treated with NPs at conc. 10 µl; (**c**) L929 cells treated with NPs at conc. 100 µl; (**d**) untreated HT29 cells; (**e**) HT29 cells treated with NPs at 10 µl; (**f**) HT29 cells treated with NPs at 100 µl. The red circle represents shrinking and morphological changes

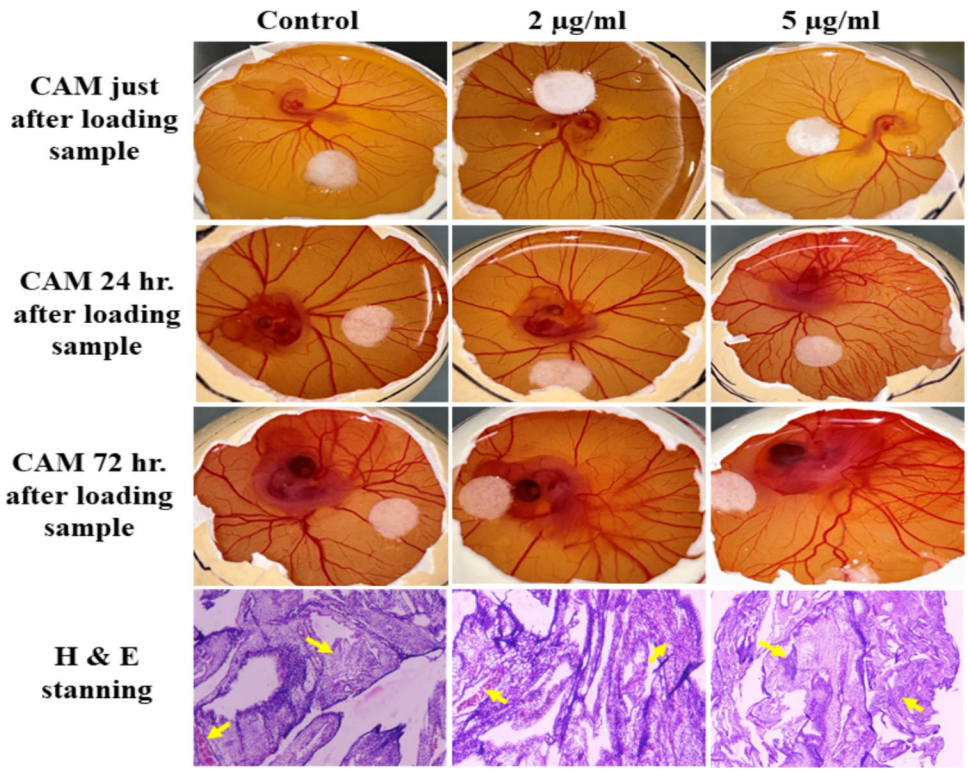

Fig. 8 Angiogenic activity of Fe_3O_4-NPs and histological analysis of CAM using H&E staining. The yellow arrow represents the formation of the formation of new vessels

performed after 72 h to further verify the new blood vessel formation of the synthesized Nps, indicating that the NPs are not harmful to the development of chick embryos, as shown in Fig. 8. The image of CAM assay of the control and treatment groups were compared and analyzed by using AngioTool v.0.6. The original and processed pictures of the CAM experiment are shown in Fig. 9a. Fe_3O_4-NPs had a strong angiogenic impact when compared to the control,

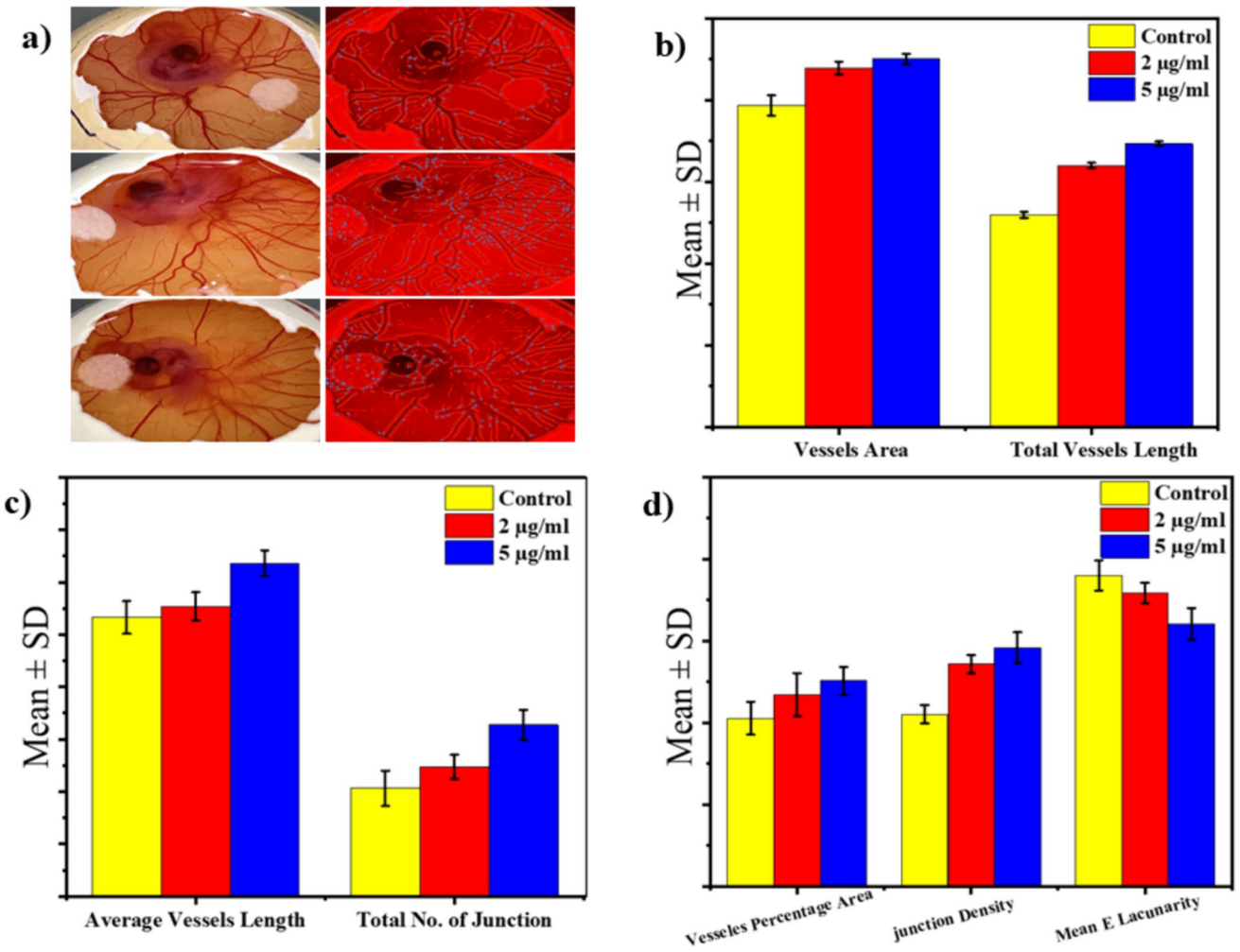

Fig. 9 Angiogenesis analysis of Fe_3O_4-NPs-treated CAM by using AngioTool software. **a** Original CAM images of control and treatment (right) and the resultant skeletonized images after processing (left). **b** CAM analysis of control and treatment with respect to vessel area and total vessel length; (**c**) analysis of the CAM by control and Fe_3O_4-NPs with respect to total number of junctions and average vessel length; (**d**) fractal analysis with vessel percentage area, junction density, and mean lacunarity of control and test

influenced vessel area and total vessel length, as shown in Fig. 9b. Analysis of the CAM by control and Fe_3O_4-NPs with respect to the total number of junctions and average vessel length is shown in Fig. 9c. The total number of connections, total vessel length, and average vessel length differed significantly between the control and treatment groups. The Fe_3O_4-NPs exhibited angiogenesis activity which was analyzed by fractal analysis. The observational studies for the same were determined by junction density, vessel percentage area, and lacunarity measurements. The difference between the control and treatment groups demonstrated Fe_3O_4-NPs angiogenic action, as shown in Fig. 9d. In this study, vascular density is directly related to angiogenesis since Fe_3O_4-NPs treatment increases vascular density when compared to a control. Furthermore, lacunarity expresses the gap distribution. The lacunarity reflects the distribution of gaps in the fractal, with higher lacunarity indicating larger gaps. In this investigation, the Fe_3O_4-NPs had low lacunarity values compared to the control.

3.6 Studies on the Lethality of Fe_3O_4-NPs on Brine Shrimp

The cytotoxic effect of a bioactive chemical on cells was evaluated in this work using the brine shrimp lethality assay, a commonly utilized method to determine the toxicity of substances. The assay produced significant insights on the possible toxicity of the chemical. Furthermore, the study was interested in investigating the effects of Fe_3O_4-NPs toxicity toward brine shrimp nauplii and its solubility in seawater. This investigation aimed to understand the chemical and toxicological effects of Fe_3O_4-NPs on marine microorganisms [51], and to document the mortality rate of biosynthesized Fe_3O_4-NPs, the concentrations used were

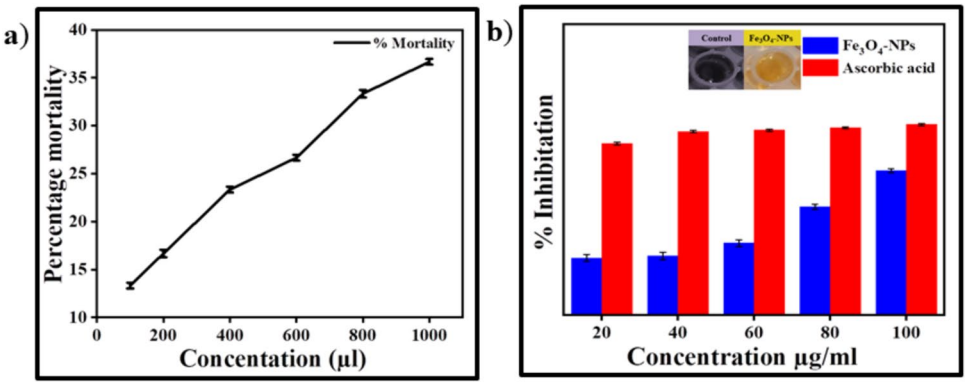

Fig. 10 **a** Percentage mortality of Fe_3O_4-NPs for different concentrations; (**b**) the graph represents the percentage inhibition of ascorbic acid and Fe_3O_4-NPs

100–1000 µl. The results showed that lethality was directly proportional to the concentration of the sample. The lowest lethality rate of 13.33% was observed at a concentration of 100 µl. This means that an increase in concentration resulted in higher cytotoxicity, indicating that the compound becomes more toxic as its concentration increases shown in Fig. 10a. However, it is worth noting that the synthesized Fe_3O_4-NPs exhibited lower mortality overall. This suggests that these NPs may have relatively low toxicity compared to other compounds or materials tested in similar studies. Overall, the findings of this study highlight the importance of considering concentration when assessing the toxicity of compounds and provide valuable insights into the toxicity of Fe_3O_4-NPs towards marine microorganisms.

3.7 Free Radical Scavenging Assay of Fe_3O_4-NPs

Evaluation of the antioxidative properties of Fe_3O_4-NPs was conducted through the DPPH free radical scavenging assay, a commonly employed method for assessing the antioxidant activity of substances. When the stable free radical DPPH interacts with Fe_3O_4-NPs, a chemical reaction occurs resulting in a color change from violet to yellow. This alteration in color serves as an indication of the hydrogen donation

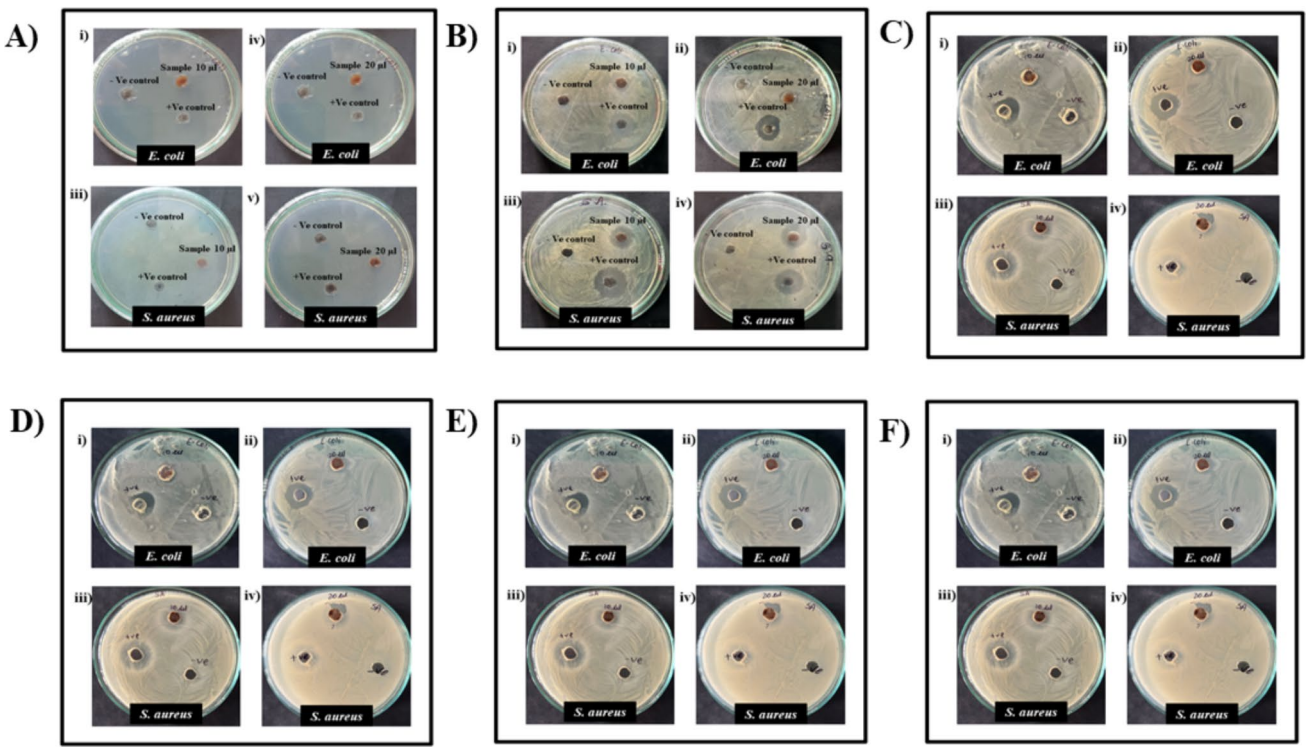

Fig. 11 Inhibitory effects of Fe_3O_4-NPs against Gram-positive and Gram-negative bacteria. **a** Zone of inhibition: 0-h incubation; (**b**) after a 6-h incubation; **c** after a 12-h incubation; (**d**) after a 24-h incubation; (**e**) 48-h incubation; (**f**) 72-h incubation

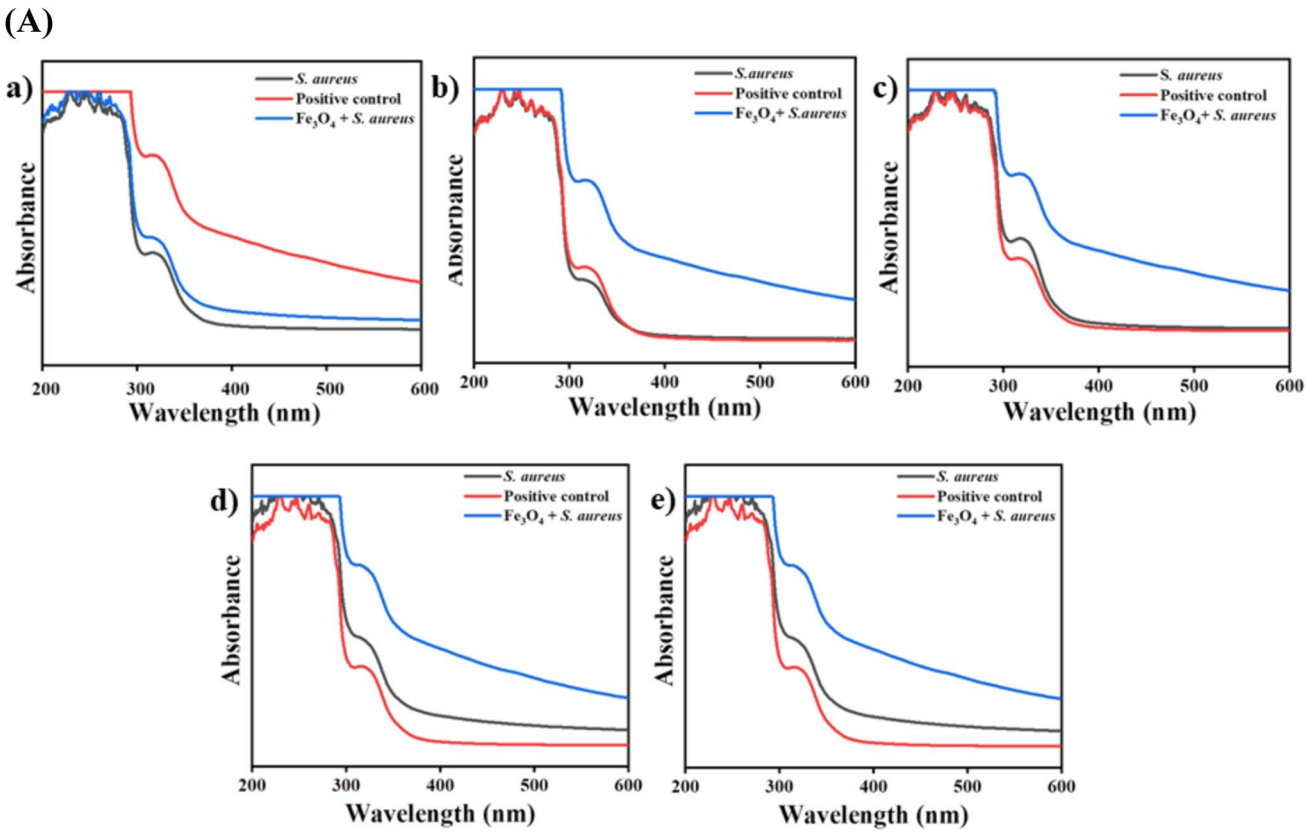

Fig. 12 Inhibitory effect of *S. aureus* using Fe_3O_4-NPs with various time intervals: (**a**) 0 h; (**b**) 6 h; (**c**) 12 h; (**d**) 24 h; (**e**) 48 h

and free radical scavenging capabilities of the antioxidant Fe_3O_4-NPs [52]. The deep violet color of DPPH is a result of electron delocalization, which is characterized by an absorption band at approximately 517 nm in an ethanol solution. However, when DPPH is mixed with a substrate capable of donating a hydrogen atom, the reduced form of DPPH is formed, leading to the loss of the violet color. This reduction reaction can be measured using a UV–vis spectrometer, which allows for the quantification of the antioxidant activity. In this study, five different concentrations (20, 40, 60, 80, and 100 µg/mL) of Fe_3O_4-NPs were used for the antioxidant assay. It was observed that the antioxidant effect increased in a dose-dependent manner, meaning that higher concentrations of Fe_3O_4-NPs resulted in greater scavenging of the DPPH free radicals. For example, at a concentration of 20 µg/mL, the free radical scavenging effect of Fe_3O_4-NPs was measured to be 23.44%. However, at a concentration of 100 µg/mL, the scavenging effect increased to 63.78%. These results indicate that Fe_3O_4-NPs possess significant antioxidant activity. In fact, the antioxidant effect of Fe_3O_4-NPs was found to be comparable or even superior to that of the standard, as shown in Fig. 10b. This suggests that Fe_3O_4-NPs could be a promising candidate for further investigation and potential use as an antioxidant in various applications.

3.8 Inhibitory Effect of Fe_3O_4-NPs on Microbial Growth

The Fe_3O_4-NPs showed inhibitory effects against pathogenic Gram-positive (*S. aureus*) and Gram-negative strains (*E. coli*) using the well diffusion method, which clearly indicates that these NPs are effective antibacterial agents. In this study, two different concentrations, like 10 µl and 20 µl of Fe_3O_4-NPs, were used**.** Fe_3O_4-NPs exhibit antibacterial activity through two mechanisms: first, the metal nanoparticles have positive charges, while bacterial cells have negative charges, which create the electromagnetic attraction between the Fe_3O_4-NPs and the microorganisms. The microorganisms oxidize and die rapidly when attraction occurs. Nanomaterials release ions that react with the thiol groups (-SH) of proteins on the bacterial cell surface, causing cell lysis. The second process is the production of ROS, which includes radicals such as hydroxyl radicals (-OH), superoxide radicals ($O2^-$), singlet oxygen ($^1O2$), and hydrogen peroxide (H_2O_2) that damage microbial cell membranes, proteins, and DNA in bacteria. ROS has inhibited a significant

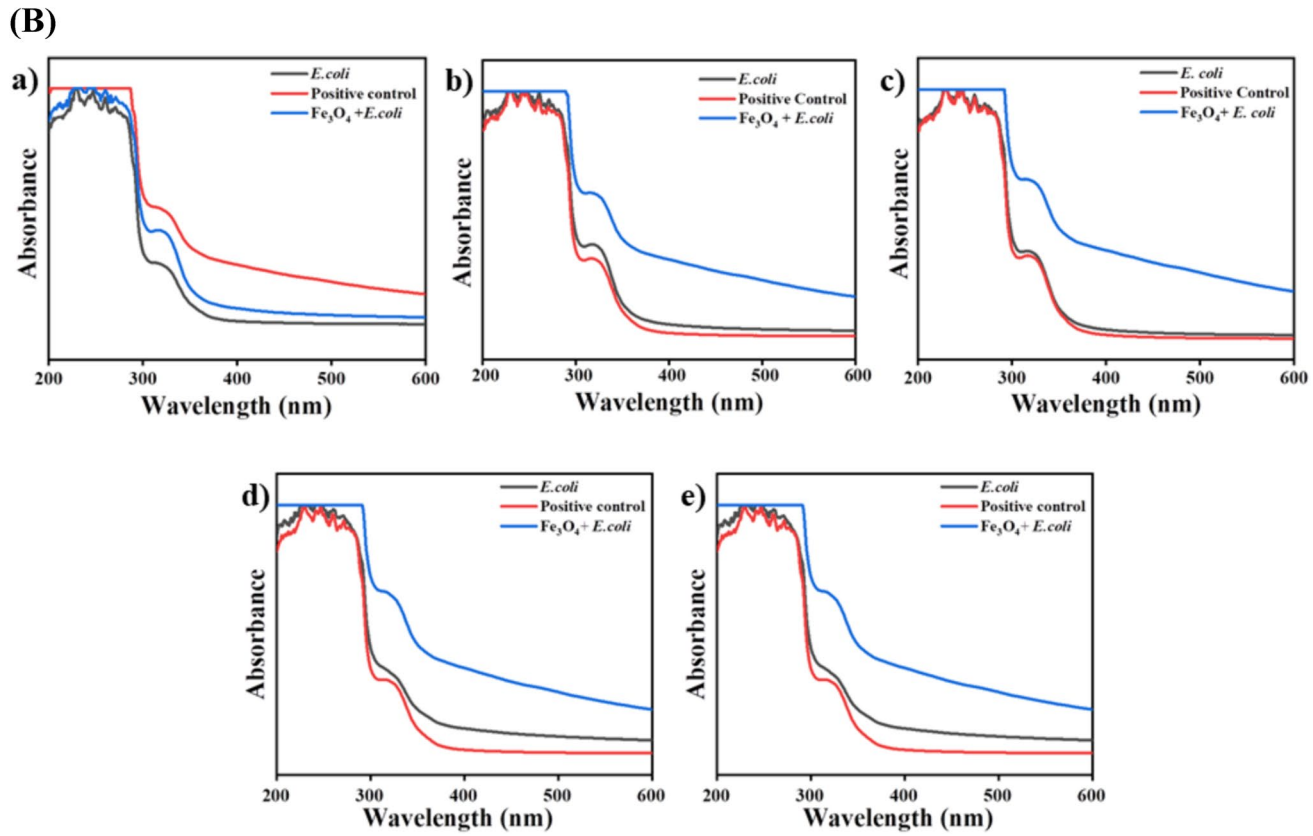

Fig. 13 Inhibitory effect of *E. coli* using Fe_3O_4-NPs with different time intervals: (**a**) 0 h; (**b**) 6 h; (**c**) 12 h; (**d**) 24 h; (**e**) 48 h

proportion of harmful bacteria generated by the present metal oxide (Fe_3O_4-NPs) [53].

The results revealed that the diameter of inhibition zones around each well with Fe_3O_4-NPs is represented in Table S1A, B. Figure 11a shows the inhibitory effect of Fe_3O_4-NPs against Gram-positive *S. aureus* and Gram-negative *E. coli* after a 0-h incubation. The positive and negative controls are also maintained, in which no zone of inhibition is observed in the positive control, negative control, or sample. 0-h time incubation of antimicrobial activity typically, when testing the antimicrobial activity of a substance, needs a certain amount of time to incubate and interact with microbes [54]. If there was no incubation time at all, the antimicrobial substance would not have a chance to act against the microbes, and thus there would not be any significant result because incubation time allows the antimicrobial agent to work on the microbes, and the results are usually measured after this period. The positive and negative controls are also maintained, and no zone of inhibition is observed in the negative control. In Fig. 11b, c, antimicrobial activity was observed at 6-h and 12-h incubation against *E. coli* and *S. aureus* in two different concentrations maintained above; slightly increasing the zone of inhibition depending on concentrations. In Fig. 11d, the antimicrobial activity was observed at a 24-h incubation against *E. coli* and *S. aureus*, which shows that in two different concentrations, the zone of inhibition increases depending on the concentration. Typically, during a 24-h incubation period, in this study, we observe the inhibition or killing effect of the antimicrobial agent, i.e., Fe_3O_4-NPs, on the microorganisms being tested. The clear zone observed around the well-called zone of inhibition indicates the effectiveness of the antimicrobial agent as Fe_3O_4-NPs. In Fig. 11e, f, antimicrobial activity was observed at 48-h and 72-h incubation against *E. coli* and *S. aureus* no increasing the zone of inhibition. After 24 h of incubation against *E. coli*, *S. aureus* shows the zone of inhibition remains constant at 48 h and 72 h. The Fe_3O_4-NPs maintain a consistent and sustained antimicrobial effect against both *E. coli* and *S. aureus* over the 24-h period. The constant zone of inhibition produced by the steady interaction between bacteria and Fe_3O_4-NPs remains stable.

3.9 Inhibitory Effect of Fe_3O_4-NPs at Time Interval Method

Fe_3O_4-NPs have been shown to have two probable modes of action against Gram-positive and Gram-negative bacteria. Because these Fe_3O_4-NPs are relatively stable in the ambient

environment, metal ion release plays a lesser role in antibacterial action. In contrast, UV triggers the synthesis of reactive oxygen species from Fe_3O_4-NPs defect sites, or visible light electron–hole pairs are formed. Electron hole pairs can generate reactive oxygen species, including superoxide radical anions (O2-) and hydroxyl radicals (OH−). Free radicals, such as O2- and OH−, can desorb membranes and kill bacteria [41]. Furthermore, many interactions, such as electrostatic, dipole–dipole, hydrogen bond, hydrophobic, and van der Wall interactions, cause disruption of cellular function as well as membrane rupture and disorganization. Bactericidal action was seen in 0-h, 6-h, 12-h, 24-h, and 48-h intervals for all bacteria combinations, as shown in Figs. 12 and 13. of Gram-positive and Gram-negative strains. Fe_3O_4-NPs had an instantaneous effect on Gram-positive and Gram-negative strains after 6, 12, and 24 h. The primary bactericidal effect of Fe_3O_4-NPs is caused by irreversible membrane-disruptive damage, which, according to the mechanism of action of Fe_3O_4-NPs, is expected to exhibit antibacterial action extremely quickly, within the initial minutes of interaction.

4 Conclusion

Fe_3O_4-NPs were effectively produced through the coprecipitation technique. Various characteristic methods were utilized to analyze the structural, morphological, and functional features. Moreover, the antibacterial and antioxidant properties of the synthesized Fe_3O_4-NPs were explored, exhibiting an inhibitory effect against *E. coli* and *S. aureus*. The efficacy of Fe_3O_4-NPs as an antioxidant agent, with 63.78% inhibition, was determined using the DPPH assay. It was deduced that the synthesized particles efficiently scavenged free radicals and prevented oxidative damage to cells, making them suitable for in vitro applications. The Fe_3O_4-NPs were evaluated for their selective anti-cancer potential against colon cancer cell lines. Cancer cells are known to produce reactive oxygen species (ROS) abundantly, which harms neighboring healthy cells. A brine shrimp lethality test indicated low levels of toxicity. This indicates that the brine shrimp subjected to the substance under examination did not suffer substantial harm or mortality due to the exposure. In conclusion, the test implies that the substance is not extremely harmful to living beings, at least within the tested concentrations. The evaluation of in ovo cytotoxicity, showing no antiangiogenic activity in CAM, is a positive indication of their biocompatibility. The small crystallite size of the synthesized Fe_3O_4-NPs displayed notable photocatalytic activity due to their higher volume-to-surface area ratio, providing active sites for reactive molecular interactions. These NPs effectively degraded the carcinogenic dyes methylene blue, fluorescein cyanine, and eosin, achieving degradation rates of 80.30%, 97.02%, and 86.83%, respectively. The investigational study demonstrated a pseudo-first-order kinetic model. At last, it can be concluded that the synthesized Fe_3O_4-NPs are environmentally friendly and biocompatible.

Supplementary Information The online version contains supplementary material available at https://doi.org/10.1007/s12668-024-01536-4.

Acknowledgements The work acknowledges D. Y. Patil Education Society (Deemed to be University), Kolhapur, India, for funding support through the intramural project (DYPES/DU/R&D/2023/1165), "*Lactobacillus Species* Loaded with Magnetite Nanoparticles for Anticancer Activity in Colon."

Author Contribution APP carried out an investigation and formal analysis, data curation, and original draft writing. PAK carried out the formal analysis and data correction of the manuscript. APT provided resources and formal analysis. AVM and UVS provided resources and formal analysis. VMK provided resources and formal analysis and carried out modification, creation, presentation, and visualization of the manuscript. ARP carried out funding acquisition, administration, supervision, and manuscript editing.

Funding This study was funded by the D. Y. Patil Education Society (Deemed to be University), Kolhapur (grant no. DYPES/DU/R&D/2023/1165) "*Lactobacillus Species* Loaded with Magnetite Nanoparticles for Anticancer Activity in Colon."

Data Availability The dataset generated and/or analyzed during the current study is available from the corresponding author on reasonable request.

Declarations

Informed Consent All authors contributed to the article and approved the submitted version for publication.

Research Involving Humans and Animals Statement The ethical approval was received from the Ethics Committee (Reg. no. ECR/738/Inst/MH/2015/RR-21) of D. Y. Patil Education Society (Deemed to be University), Kolhapur, Maharashtra, India.

Conflict of Interest None.

References

1. Bayda, M. A.,Tuccinardi, T., Cordani, M., & Rizzolio, F. (2020). Molecules-25-00112-V2.Pdf. *Molecules, 25*, 1–15. https://doi.org/10.3390/molecules25010112
2. Tabasi, H., Hamed Mosavian, M. T., Sabouri, Z., Khazaei, M., & Darroudi, M. (2021). pH-responsive and CD44-targeting by Fe3O4/MSNs-NH2 nanocarriers for oxaliplatin loading and colon cancer treatment. *Inorg Chem Commun,125*, 108430. https://doi.org/10.1016/j.inoche.2020.108430
3. Ezealigo, U. S., Ezealigo, B. N., Aisida, S. O., & Ezema, F. I. (2021). Iron oxide nanoparticles in biological systems: Antibacterial and toxicology perspective. *JCIS Open,4*, 100027. https://doi.org/10.1016/j.jciso.2021.100027
4. Sangaiya, P., & Jayaprakash, R. (2018). A review on iron oxide nanoparticles and their biomedical applications. *Journal of Superconductivity and Novel Magnetism,31*, 3397–3413. https://doi.org/10.1007/s10948-018-4841-2

5. AL-Harbi, L. M., Darwish, M. S. A. (2022). Functionalized iron oxide nanoparticles: Synthesis through ultrasonic-assisted co-precipitation and performance as hyperthermic agents for biomedical applications. *Heliyon, 8*, e09654. https://doi.org/10.1016/j.heliyon.2022.e09654
6. Tabassum, N., Singh, V., Chaturvedi, V. K., Vamanu, E., & Singh, M. P. (2023). A facile synthesis of flower-like iron oxide nanoparticles and its efficacy measurements for antibacterial, cytotoxicity and antioxidant activity. *Pharmaceutics,15*, 1726. https://doi.org/10.3390/pharmaceutics15061726
7. Besenhard, M. O., LaGrow, A. P., Hodzic, A., Kriechbaum, M., Panariello, L., Bais, G., Loizou, K., Damilos, S., Margarida Cruz, M., Thanh, N. T. K., & Gavriilidis, A. (2020). Co-precipitation synthesis of stable iron oxide nanoparticles with NaOH: New insights and continuous production via flow chemistry. *Chem. Eng. J.,399*, 125740. https://doi.org/10.1016/j.cej.2020.125740
8. Ali, A., Zafar, H., Zia, M., ul Haq, I., Phull, A. R., Ali, J. S., & Hussain, A. (2016). Synthesis, characterization, applications, and challenges of iron oxide nanoparticles. *Nanotechnol. Sci. Appl,9*, 49–67. https://doi.org/10.2147/NSA.S99986
9. Marimuthu, S., Antonisamy, A. J., Malayandi, S., Rajendran, K., Tsai, P.-C., Pugazhendhi, A., & Ponnusamy, V. K. (2020). Silver nanoparticles in dye effluent treatment: A review on synthesis, treatment methods, mechanisms, photocatalytic degradation, toxic effects and mitigation of toxicity. *Journal of Photochemistry and Photobiology, B: Biology,205*, 111823. https://doi.org/10.1016/j.jphotobiol.2020.111823
10. Kamaraj, M., Kidane, T., Muluken, K. U., & Aravind, J. (2019). Biofabrication of iron oxide nanoparticles as a potential photocatalyst for dye degradation with antimicrobial activity. *International Journal of Environmental Science and Technology,16*, 8305–8314. https://doi.org/10.1007/s13762-019-02402-7
11. Mehra, S., Singh, M., & Chadha, P. (2021). Adverse impact of textile dyes on the aquatic environment as well as on human beings. *Toxicol Int,28*, 165–176. https://doi.org/10.18311/ti/2021/v28i2/26798
12. Haritha, E., Roopan, S. M., Madhavi, G., Elango, G., Al-Dhabi, N. A., & Arasu, M. V. (2016). Green chemical approach towards the synthesis of SnO 2 NPs in argument with photocatalytic degradation of diazo dye and its kinetic studies. *Journal of Photochemistry and Photobiology, B: Biology,162*, 441–447. https://doi.org/10.1016/j.jphotobiol.2016.07.010
13. Yaou Balarabe, B., Illiassou Oumarou, M. N., Koroney, A. S., Adjama, I., & Ibrahim Baraze, A. R. (2023) Photo-oxidation of organic dye by Fe2O3 nanoparticles: catalyst, electron acceptor, and polyurethane membrane (PU-Fe2O3) effects. *Journal of Nanotechnology*, 1–12. https://doi.org/10.1155/2023/1292762.
14. Ghanimati, M., Abdoli-Senejani, M., Bodaghifard, M. A., & Momeni Isfahani, T. (2020). Phosphomolybdic acid immobilized chitosan/Fe3O4: an efficient catalyst for n alkylation of anilines. *Eurasian Chemical Communications, 2*, 688–701. https://doi.org/10.33945/SAMI/ECC.2020.6.6
15. Revathy, R., Sajini, T., Augustine, C., & Joseph, N. (2023). Iron-based magnetic nanomaterials: Sustainable approaches of synthesis and applications. *Results in Engineering,18*, 101114. https://doi.org/10.1016/j.rineng.2023.101114
16. Nosaka, Y., & Nosaka, A. Y. (2017). Generation and detection of reactive oxygen species in photocatalysis. *Chemical Reviews,117*, 11302–11336. https://doi.org/10.1021/acs.chemrev.7b00161
17. Kumar, A. P., Bilehal, D., Desalegn, T., Kumar, S., Ahmed, F., Murthy, H. C. A., Kumar, D., Gupta, G., Chellappan, D. K., Singh, S. K., Dua, K., & Lee, Y.-I. (2022). Studies on synthesis and characterization of Fe 3 O 4 @SiO 2 @Ru hybrid magnetic composites for reusable photocatalytic application. *Adsorption Science & Technology,2022*, 1–18. https://doi.org/10.1155/2022/3970287
18. Nami, N., Tajbakhsh, M., & Vafakhah, M. (2019). Application and comparison of the catalytic activity of Fe3O4MNPs, kaolin and montmorillonite K10 for the synthesis of indole derivatives. *Iranian Chemical Communication,1*, 93–101. https://doi.org/10.33945/SAMI/ECC.2019.1.8
19. Ribeiro, M., Boudoukhani, M., Belmonte-Reche, E., Genicio, N., Sillankorva, S., Gallo, J., Rodríguez-Abreu, C., Moulai-Mostefa, N., & Bañobre-López, M. (2021). Xanthan-Fe3O4 nanoparticle composite hydrogels for non-invasive magnetic resonance imaging and magnetically assisted drug delivery. *ACS Appl. Nano Mater.,4*, 7712–7729. https://doi.org/10.1021/acsanm.1c00932
20. Vassallo, M., Martella, D., Barrera, G., Celegato, F., Coïsson, M., Ferrero, R., Olivetti, E. S., Troia, A., Sözeri, H., Parmeggiani, C., Wiersma, D. S., Tiberto, P., & Manzin, A. (2022). Improvement of hyperthermia properties of iron oxide nanoparticles by surface coating. *ACS Omega,6*, 2143–2154. https://doi.org/10.1021/acsomega.2c06244
21. Bai, C., Hu, P., Liu, N., Feng, G., Liu, D., Chen, Y., Ma, M., Gu, N., & Zhang, Y. (2020). Synthesis of ultrasmall Fe3O4 nanoparticles as T1–T2 dual-modal magnetic resonance imaging contrast agents in rabbit hepatic tumors. *ACS Appl. Nano Mater.,3*, 3585–3595. https://doi.org/10.1021/acsanm.0c00306
22. Liou, G. Y., & Storz, P. (2010). *Reactive oxygen species in cancer*. https://doi.org/10.3109/10715761003667554
23. Rajabi, S., Ramazani, A., Hamidi, M., & Naji, T. (2015). Artemia salina as a model organism in toxicity assessment of nanoparticles, DARU. *Journal of Pharmaceutical Sciences,23*, 1–6. https://doi.org/10.1186/s40199-015-0105-x
24. Krysanov, E. Y., Pavlov, D. S., Demidova, T. B., & Dgebuadze, Y. Y. (2010). Effect of nanoparticles on aquatic organisms. *Biological Bulletin,37*, 406–412. https://doi.org/10.1134/S1062359010040114
25. Alkhayal, A., Fathima, A., Alhasan, A. H., & Alsharaeh, E. H. (2021). PEG coated Fe3O4/RGO nano-cube-like structures for cancer therapy via magnetic hyperthermia. *Nanomaterials,11*, 2398. https://doi.org/10.3390/nano11092398
26. Asab, G., Zereffa, E. A., & Abdo Seghne, T. (2020). Synthesis of silica-coated Fe 3 O 4 nanoparticles by microemulsion method: characterization and evaluation of antimicrobial activity. *Int. J. Biomater.,2020*, 1–11. https://doi.org/10.1155/2020/4783612
27. Imran, M., Riaz, S., Shah, S. M. H., Batool, T., Khan, H. N., Sabri, A. N., & Naseem, S. (2020). In-vitro hemolytic activity and free radical scavenging by sol-gel synthesized Fe3O4 stabilized ZrO2 nanoparticles. *Arabian Journal of Chemistry,13*, 7598–7608. https://doi.org/10.1016/j.arabjc.2020.08.027
28. Dorniani, D., Kura, A. U., Ahmad, Z., Halim Shaari, A., Hussein, M. Z., & Fakurazi, S. (2012). Preparation of Fe3O4 magnetic nanoparticles coated with gallic acid for drug delivery. *Int. J. Nanomedicine,7*, 5745. https://doi.org/10.2147/IJN.S35746
29. Kozenkova, E., Levada, K., Efremova, M. V., Omelyanchik, A., Nalench, Y. A., Garanina, A. S., Pshenichnikov, S., Zhukov, D. G., Lunov, O., Lunova, M., Kozenkov, I., Innocenti, C., Albino, M., Abakumov, M. A., Sangregorio, C., & Rodionova, V. (2020). Multifunctional Fe3O4-Au Nanoparticles for the MRI diagnosis and potential treatment of liver cancer. *Nanomaterials,10*, 1646. https://doi.org/10.3390/nano10091646
30. Petcharoen, K., & Sirivat, A. (2012). Synthesis and characterization of magnetite nanoparticles via the chemical co-precipitation method. *Materials Science and Engineering B,177*, 421–427. https://doi.org/10.1016/j.mseb.2012.01.003
31. Gambhir, R. P., Kale, S., Dongale, T., Patil, S., Malavekar, D., & Tiwari, A. P. (2023). Green synthesized magnetic nanoparticles

for selective inhibition of osteosarcoma cancer. *J. Nanoparticle Res.,25*, 1–14. https://doi.org/10.1007/s11051-023-05735-0
32. Sarala, E., Madhukara Naik, M., Vinuth, M., Rami Reddy, Y. V., & Sujatha, H. R. (2020). Green synthesis of Lawsonia inermis-mediated zinc ferrite nanoparticles for magnetic studies and anticancer activity against breast cancer (MCF-7) cell lines. *J. Mater. Sci. Mater. Electron.,31*, 8589–8596. https://doi.org/10.1007/s10854-020-03394-8
33. Karuppaiya, P., Satheeshkumar, E., & Tsay, H. S. (2019). Biogenic synthesis of silver nanoparticles using rhizome extract of Dysosma pleiantha and its antiproliferative effect against breast and human gastric cancer cells. *Molecular Biology Reports,46*, 4725–4734. https://doi.org/10.1007/s11033-019-04917-1
34. Mitrevska, K., Merlos Rodrigo, M. A., Cernei, N., Michalkova, H., Splichal, Z., Hynek, D., Zitka, O., Heger, Z., Kopel, P., Adam, V., & Milosavljevic, V. (2023). Chick chorioallantoic membrane (CAM) assay for the evaluation of the antitumor and antimetastatic activity of platinum-based drugs in association with the impact on the amino acid metabolism. *Mater. Today Bio,19*, 100570. https://doi.org/10.1016/j.mtbio.2023.100570
35. Safawo, T., Sandeep, B., Pola, S., & Tadesse, A. (2018). Synthesis and characterization of zinc oxide nanoparticles using tuber extract of anchote (Coccinia abyssinica (Lam.) Cong.) for antimicrobial and antioxidant activity assessment. *OpenNano,3*, 56–63. https://doi.org/10.1016/j.onano.2018.08.001
36. Ayesha, M., Imran, A., Haider, I., Shahzadi, S., Moeen, A., Ul-Hamid, W., Nabgan, A., Shahzadi, T., & Alshahrani, M. (2023). Ikram, Polyvinylpyrrolidone and chitosan-coated magnetite (Fe3O4) nanoparticles for catalytic and antimicrobial activity with molecular docking analysis. *Journal of Environmental Chemical Engineering,11*, 110088. https://doi.org/10.1016/j.jece.2023.110088
37. Tavares, T. D., Antunes, J. C., Padrão, J., Ribeiro, A. I., Zille, A., Amorim, M. T. P., Ferreira, F., & Felgueiras, H. P. (2020). Activity of specialized biomolecules against gram-positive and gram-negative bacteria. *Antibiotics,9*, 1–16. https://doi.org/10.3390/antibiotics9060314
38. Wardani, R. K., Dahlan, K., Wahyudi, S. T., & Sukaryo, S. G. (2019). Synthesis and characterization of nanoparticle magnetite for biomedical application. In *AIP Conference Proceedings* (pp. 020137). https://doi.org/10.1063/1.5139869
39. Yusoff, A. H. M., Salimi, M. N., & Jamlos, M. F. (2017). Synthesis and characterization of biocompatible Fe3O4 nanoparticles at different pH. In *AIP Conference Proceedings* (pp. 020010). https://doi.org/10.1063/1.4981832
40. Fadli, A., Komalasari, Adnan, A., Iwantono, Rahimah, Addabsi, A. S. (2019). Synthesis of magnetite nanoparticles via co-precipitation method. *IOP Conference Series: Materials Science and Engineering, 622*. https://doi.org/10.1088/1757-899X/622/1/012013
41. Tabasi, H., Mosavian, M. T. H., Darroudi, M., Khazaei, M., Hashemzadeh, A., & Sabouri, Z. (2022). Synthesis and characterization of amine-functionalized Fe3O4/mesoporous silica nanoparticles (MSNs) as potential nanocarriers in drug delivery systems. *Journal of Porous Materials,29*, 1817–1828. https://doi.org/10.1007/s10934-022-01259-5
42. Mobasherat Jajroud, S. Y., Falahati, M., Attar, F., & Khavari-Nejad, R. A. (2018). Human hemoglobin adsorption onto colloidal cerium oxide nanoparticles: a new model based on zeta potential and spectroscopy measurements. *J. Biomol. Struct. Dyn.,36*, 2908–2916. https://doi.org/10.1080/07391102.2017.1371645
43. Rahman, M. M., Hussain, M. M., & Asiri, A. M. (2017). Fabrication of 3-methoxyphenol sensor based on Fe3O4 decorated carbon nanotube nanocomposites for environmental safety: Real sample analyses. *PLoS ONE,12*, 1–15. https://doi.org/10.1371/journal.pone.0177817
44. Sabouri, Z., Sammak, S., Sabouri, S., Moghaddas, S. S. T. H., & Darroudi, M. (2024). Green synthesis of Ag-Se doped ZnO-Co3O4-NiO fivenary nanocomposite using poly anionic cellulose and evaluation of their anticancer and photocatalyst applications. *Chemical Methodologies, 8*, 164–176. https://doi.org/10.48309/chemm.2024.436507.1758
45. Thy, L. T. M., Cuong, P. M., Tu, T. H., Nam, H. M., Hieu, N. H., & Phong, M. T. (2020). Fabrication of magnetic iron oxide/graphene oxide nanocomposites for removal of lead ions from water. *Chemical Engineering Transactions,78*, 277–282. https://doi.org/10.3303/CET2078047
46. Sabouri, Z., Sabouri, M., Moghaddas, S. S. T. H., Mostafapour, A., Samarghandian, S., Darroudi, M. (2023). Plant-mediated synthesis of Ag and Se dual-doped ZnO-CaO-CuO nanocomposite using Nymphaea alba L. extract: assessment of their photocatalytic and biological properties. *Biomass Conversion and Biorefinery*, 1–11. https://doi.org/10.1007/S13399-023-04984-2/METRICS
47. Albeladi, A., Khan, Z., Al-Thabaiti, S. A., Patel, R., Malik, M. A., & Mehta, S. (2024). Fe3O4-CdO nanocomposite for organic dye photocatalytic degradation: Synthesis and characterization. *Catalysts,14*, 71. https://doi.org/10.3390/catal14010071
48. Sabouri, Z., Sabouri, M., Moghaddas, S. S. T. H., & Darroudi, M. (2023). Design and preparation of amino-functionalized core-shell magnetic nanoparticles for photocatalytic application and investigation of cytotoxicity effects. *J. Environ. Heal. Sci. Eng.,21*, 93–105. https://doi.org/10.1007/S40201-022-00842-X/METRICS
49. Wang, K., Hu, H., Zhang, Q., Zhang, Y., & Shi, C. (2019). Synthesis, purification, and anticancer effect of magnetic Fe 3 O 4 -loaded poly (lactic-co-glycolic) nanoparticles of the natural drug tetrandrine. *Journal of Microencapsulation,36*, 356–370. https://doi.org/10.1080/02652048.2019.1631403
50. Alfareed, T. M., Slimani, Y., Almessiere, M. A., Nawaz, M., Khan, F. A., Baykal, A., & Al-Suhaimi, E. A. (2022). Biocompatibility and colorectal anti-cancer activity study of nanosized BaTiO3 coated spinel ferrites. *Science and Reports,12*, 1–18. https://doi.org/10.1038/s41598-022-18306-5
51. Zhu, S., Xue, M.-Y., Luo, F., Chen, W.-C., Zhu, B., & Wang, G.-X. (2017). Developmental toxicity of Fe 3 O 4 nanoparticles on cysts and three larval stages of Artemia salina. *Environmental Pollution,230*, 683–691. https://doi.org/10.1016/j.envpol.2017.06.065
52. Baliyan, S., Mukherjee, R., Priyadarshini, A., Vibhuti, A., Gupta, A., Pandey, R. P., & Chang, C.-M. (2022). Determination of antioxidants by DPPH radical scavenging activity and quantitative phytochemical analysis of Ficus religiosa. *Molecules,27*, 1326. https://doi.org/10.3390/molecules27041326
53. Prabhu, Y. T., Rao, K. V., Kumari, B. S., Kumar, V. S. S., & Pavani, T. (2015). Synthesis of Fe3O4 nanoparticles and its antibacterial application. *Int. Nano Lett.,5*, 85–92. https://doi.org/10.1007/s40089-015-0141-z
54. Laure, N. N., Dawan, J., & Ahn, J. (2021). Effects of incubation time and inoculation level on the stabilities of bacteriostatic and bactericidal antibiotics against Salmonella Typhimurium. *Antibiotics,10*, 1019. https://doi.org/10.3390/antibiotics10081019